Title

SN REFSDAL: CLASSIFICATION AS A LUMINOUS AND BLUE SN 1987A-LIKE TYPE II SUPERNOVA

Authors

Kelly, PL
Brammer, G
Selsing, J
et al.

SN REFSDAL: CLASSIFICATION AS A LUMINOUS AND BLUE SN 1987A-LIKE TYPE II SUPERNOVA

P. L. Kelly[1], G. Brammer[2], J. Selsing[3], R. J. Foley[4,5], J. Hjorth[3], S. A. Rodney[6,], L. Christensen[3], L.-G. Strolger[2], A. V. Filippenko[1], T. Treu[7,8], C. C. Steidel[9], A. Strom[9], A. G. Riess[10,2], A. Zitrin[9,11], K. B. Schmidt[12], M. Bradač[13], S. W. Jha[14], M. L. Graham[1], C. McCully[15,12], O. Graur[16,17], B. J. Weiner[18], AND J. M. Silverman[19]

Submitted to The Astrophysical Journal

ABSTRACT

We have acquired *Hubble Space Telescope (HST)* and Very Large Telescope near-infrared spectra and images of supernova (SN) Refsdal after its discovery as an Einstein cross in Fall 2014. The *HST* light curve of SN Refsdal matches the distinctive, slowly rising light curves of SN 1987A-like supernovae (SNe), and we find strong evidence for a broad $H\alpha$ P-Cygni profile in the *HST* grism spectrum at the redshift ($z = 1.49$) of the spiral host galaxy. SNe IIn, powered by circumstellar interaction, could provide a good match to the light curve of SN Refsdal, but the spectrum of a SN IIn would not show broad and strong $H\alpha$ absorption. From the grism spectrum, we measure an $H\alpha$ expansion velocity consistent with those of SN 1987A-like SNe at a similar phase. The luminosity, evolution, and Gaussian profile of the $H\alpha$ emission of the WFC3 and X-shooter spectra, separated by ~ 2.5 months in the rest frame, provide additional evidence that supports the SN 1987A-like classification. In comparison with other examples of SN 1987A-like SNe, SN Refsdal has a blue $B - V$ color and a high luminosity for the assumed range of potential magnifications. If SN Refsdal can be modeled as a scaled version of SN 1987A, we estimate it would have an ejecta mass of 20 ± 5 M$_\odot$. The evolution of the light curve at late times will provide additional evidence about the potential existence of any substantial circumstellar material (CSM). Using MOSFIRE and X-shooter spectra, we estimate a subsolar host-galaxy metallicity (8.3 ± 0.1 dex and <8.4 dex, respectively) near the explosion site.

Subject headings: gravitational lensing: strong — supernovae: general, individual: SN Refsdal — galaxies: clusters: general, individual: MACS J1149+2223

1. INTRODUCTION

pkelly@astro.berkeley.edu

[1] Department of Astronomy, University of California, Berkeley, CA 94720-3411, USA

[2] Space Telescope Science Institute, 3700 San Martin Dr., Baltimore, MD 21218, USA

[3] Dark Cosmology Centre, Niels Bohr Institute, University of Copenhagen, Juliane Maries Vej 30, DK-2100 Copenhagen, Denmark

[4] Department of Physics, University of Illinois at Urbana-Champaign, 1110 W. Green Street, Urbana, IL 61801, USA

[5] Astronomy Department, University of Illinois at Urbana-Champaign, 1002 W. Green Street, Urbana, IL 61801, USA

[6] Department of Physics and Astronomy, University of South Carolina, 712 Main St., Columbia, SC 29208, USA

[7] University of California, Los Angeles, CA 90095

[8] Packard Fellow

[9] California Institute of Technology, 1200 East California Boulevard, Pasadena, CA 91125

[10] Department of Physics and Astronomy, The Johns Hopkins University, 3400 N. Charles St., Baltimore, MD 21218, USA

[12] Department of Physics, University of California, Santa Barbara, CA 93106-9530, USA

[13] University of California, Davis, 1 Shields Avenue, Davis, CA 95616

[14] Department of Physics and Astronomy, Rutgers, The State University of New Jersey, Piscataway, NJ 08854, USA

[15] Las Cumbres Observatory Global Telescope Network, 6740 Cortona Dr., Suite 102, Goleta, California 93117, USA

[16] Center for Cosmology and Particle Physics, New York University, New York, NY 10003, USA

[17] Department of Astrophysics, American Museum of Natural History, Central Park West and 79th Street, New York, NY 10024, USA

[18] Department of Astronomy, University of Arizona, Tucson, AZ 85721, USA

[19] Department of Astronomy, University of Texas at Austin, Austin, TX 78712, USA

Refsdal (1964) first considered the possibility that a gravitational lens might create multiple images of a background supernova (SN) explosion. He showed that the time delays between the images of the SN should depend on the distribution of matter in the lens and, geometrically, on the cosmic expansion rate. In Kelly et al. (2015b), we reported the first example of a strongly lensed SN resolved into multiple images, which we found in near-infrared (NIR) *HST* WFC3 exposures of the MACS J1149+2223 cluster (Ebeling et al. 2001) taken as part of the Grism Lens-Amplified Survey from Space (GLASS; PI T. Treu; GO-13459; see Schmidt et al. 2014; Treu et al. 2015b). The data revealed a total of four images of the SN in an Einstein cross surrounding an early-type galaxy in the cluster. Here we use photometry and spectroscopy from the first year after discovery to classify the SN and characterize its basic properties.

The explosion site of SN Refsdal is close to the tip of a spiral arm of a galaxy at redshift $z = 1.49$ (Smith et al. 2009). The galaxy is inclined at an angle of $i = 45 \pm 10°$ (Yuan et al. 2011) and is multiply imaged (Zitrin & Broadhurst 2009) by the potential of the massive MACS J1149+2223 cluster [$(1.4 \pm 0.3) \times 10^{15}$ M$_\odot$; von der Linden et al. 2014; Kelly et al. 2014; Applegate et al. 2014] at $z = 0.54$. The cluster lens forms three images of the SN host galaxy that include the explosion site of the SN.

Light that travels toward us on a direct route through the center of the cluster arrives last owing to the greater spatial curvature and gravitational time dilation near the center of the potential (see Treu & Ellis 2015 for a re-

view). In Kelly et al. (2015b), we predicted that the 2014 appearances were only the next-to-last arrival and that the SN would reappear within several years closer to the center of the cluster. Modeling efforts (Oguri 2015; Sharon & Johnson 2015; Diego et al. 2015) sought to make more precise predictions by collecting improved datasets (Jauzac et al. 2015; Treu et al. 2015a; Grillo et al. 2015; Kawamata et al. 2015). An imaging campaign with *HST* (PI P. Kelly; GO-14199) detected the predicted reappearance on December 11, 2015 (UT dates are used throughout this paper; Kelly et al. 2015a), and deep follow-up images will measure the relative time delay with 1–2% precision.

Either a thermonuclear Type Ia SN or a core-collapse SN provided a reasonable match to the light curve and colors of SN Refsdal during the first month after discovery, which was made on November 11, 2014. After a 1 hr Keck-I MOSFIRE observation (PI C. Steidel) was not able to detect the SN, an *HST* Director's Discretionary (DD) time program was carried out from December 23, 2014 through January 5, 2015 (PI P. Kelly; GO-14041) to acquire WFC3 spectra. Instead of fading as would have been expected for a SN Ia, SN Refsdal continued a slow rise in brightness, which made ground-based NIR spectroscopy possible near the peak of the light curve. We obtained Very Large Telescope (VLT) X-shooter spectra through an ESO DD program (PI J. Hjorth; 295.D-5014) in May and June 2015, approximately six months after discovery. Keck-II DEIMOS observations taken in December 2015, March 2015, and May 2015 yielded no detection of the SN at optical wavelengths.

Here we show that the spectra and light curve of SN Refsdal are consistent with those of SN 1987A-like supernovae (SNe), whose prototype was the best-studied SN explosion in recent history. A companion paper (Rodney et al. 2015) presents measurements of the relative time delays and magnifications of the four images in the Einstein cross, and magnitudes measured using point-spread-function (PSF) fitting photometry. In Section 2, we describe the MOSFIRE, DEIMOS, *HST* grism, and X-shooter spectra that we have collected. The photometric classification of the light curve is discussed in Section 3. Section 4 presents an analysis of the SN spectra, and Section 5 contains measurements of the host-galaxy environment. We summarize the results in Section 6. The methods that we use to process and extract spectra of SN Refsdal are explained in detail in the Appendix.

2. DATA

2.1. *Keck-I MOSFIRE Spectra*

On November 23, 2014, approximately two weeks after discovery, we obtained a 1 hr *H*-band integration with the Multi-Object Spectrometer For Infra-Red Exploration (MOSFIRE; McLean et al. 2010, 2012) mounted on the 10 m Keck-I telescope. As we show in Figure 1, a $0\rlap{.}''7$ wide slit was oriented position angle (PA) 109.68° to place the slit across both images S1 and S2. The resolving power of the setup was $R = 3660$ in the H band (1.48–1.81 μm), chosen to be able to have sensitivity to Hα emission at the redshift (1.49) of the face-on spiral galaxy. Table 1 provides an overview of the MOSFIRE observations.

The data were obtained using mask nodding in thirty

119.29 s exposures, split evenly between integration at positions A and B separated by $12''$ along the slit in an alternating sequence, for a total integration of 3578.8 s. The full width at half-maximum intensity (FWHM) of the J-band PSF was estimated to be $0\rlap{.}''7$ during the observations, and the H-band FWHM is expected to have smaller size. The data were reduced using the MOSFIRE Data Reduction Pipeline[19].

We extract the spectra of images S1 and S2 using a 4 pixel ($0\rlap{.}''72$) width aperture centered on the expected positions of the images of the SN. The locations of S1 and S2 show narrow nebular emission from the host galaxy.

2.2. *Keck-II DEIMOS Data*

We also obtained optical spectra of the field at the 10 m Keck-II telescope using the DEIMOS spectrograph (Faber et al. 2003). We used multislit masks with $1''$ wide slits that included the positions of Refsdal images S1 and S3 on December 20, 2014 with approximately 3 hr of exposure time in fair conditions, and images S2 and S3 on March 18, 2015 (3 hr of exposure in good conditions) and May 20, 2015 (1.5 hr of exposure in moderate conditions). We used the 600-line grating with a central wavelength of 7200 Å, resulting in a wavelength range of 5000–10,000 Å at a scale of 0.65 Å per pixel. A preliminary analysis of the data using a customized version of the DEEP2 pipeline (Newman et al. 2013; Cooper et al. 2012) showed no detectable signal from SN Refsdal over the background.

2.3. *HST G141 Grism Spectra*

As a part of an *HST* DD program (GO-14041; PI P. Kelly), we obtained thirty orbits of WFC3 G141 grism spectra during the period from December 23, 2014 through January 5, 2015 (13.2 days; 5.3 days in the rest frame) when SN Refsdal had $F160W \approx 25.1$ mag AB. During the grism observations, the mean phase of the SN relative to maximum brightness was -47 ± 8 d. Each 2405.9 s G141 grism integration was followed by a WFC3 direct imaging 202.9 s integration through either the $F125W$ or the $F160W$ broad-band filters, which are used to align the grism data. The total integration was split equally between observations at telescope orientations of 111° and 119°, where the spectrum of the SN images S2 and S3 were expected to suffer the least contamination from spectra of nearby sources based on our planning simulations and knowledge of the layout of sources in the field.

The WFC3 G141 grism has a resolving power of ~ 70 Å (~ 1400 km s^{-1}), and a wavelength range of 11,000–17,000 Å (~ 4400–6800 Å in the $z = 1.49$ SN rest frame). Pointings were made using subpixel offsets to sample the WFC3 PSF completely. The first order of the WFC3 G141 grism has a maximum efficiency of 48% near 14,500 Å, while the second order reaches $\sim 8\%$ near $\sim 11,000$ Å. Each WFC3-IR image has 1024×1024 pixels covering a $136'' \times 123''$ field of view, and the spectra have an average tilt of $\sim 0.5°$ relative to the detector's axis.

2.4. *HST Light Curves*

---

[19] https://keck-datareductionpipelines.github.io/MosfireDRP/

Table 1
Details of Keck-I MOSFIRE Observations

Date (MJD)	$F160W$ AB (± 0.1 mag)	α(J2000)	δ(J2000)	Position Angle	Para. Angle	Airmass	Total Exp. (s)	Slit Width	Seeing
56984	~ 25.45 (S1); ~ 25.5 (S2)	11:49:35.574	+22:23:44.06	109.68°	82°	1.56	3578.8	0.″7	0.″7[a]

Note. — Magnitudes listed are total and do not account for slit losses, and are extrapolated from the first $F160W$ observations by ~ 6 days in the observed frame (~ 2.5 days in the rest frame). Observations were acquired in a sequence of thirty 119.29 s exposures.
[a] Determined from the J-band image; the FWHM in the H band should be smaller.

Table 2
Details of VLT X-shooter Observations

OB	Date (MJD)	$F160W$ AB (± 0.1 mag)	α(J2000)	δ(J2000)	Position Angle	Para. Angle	Airmass	Total Exp. (s)	NIR Slit Width
1	57158	24.75 (S1); 24.47 (S2)	11:49:35.520	+22:23:44.44	108.2°	175°	1.47	4800	0.″6
2	57188	24.75 (S1); 24.60 (S2)	11:49:35.511	+22:23:44.65	108.2°	165°	1.51	4800	0.″9
3	57189	24.60 (S2); 24.60 (S3)	11:49:35.406	+22:23:44.40	51.6°	162°	1.53	4800	0.″9

Note. — Magnitudes listed are total and do not account for slit losses. Observations were acquired in a sequence of four 1200 s exposures.

Table 3
Seeing During X-shooter Observation Blocks

OB	Acquisition Image (FWHM)	Estimated Average
1	0.″69	1.″00
2	0.″62	0.″7
3	0.″54	0.″9

Note. — To estimate the seeing at the beginning of each OB, two bright stars in the acquisition image are fit with a two-dimensional Gaussian. For all observations a significant worsening of the seeing occurred during the observations. To estimate the average seeing during each OB, we scale the average DIMM seeing by the difference between the measured FWHM in the acquisition images and the DIMM FWHM recorded at the beginning of the OB.
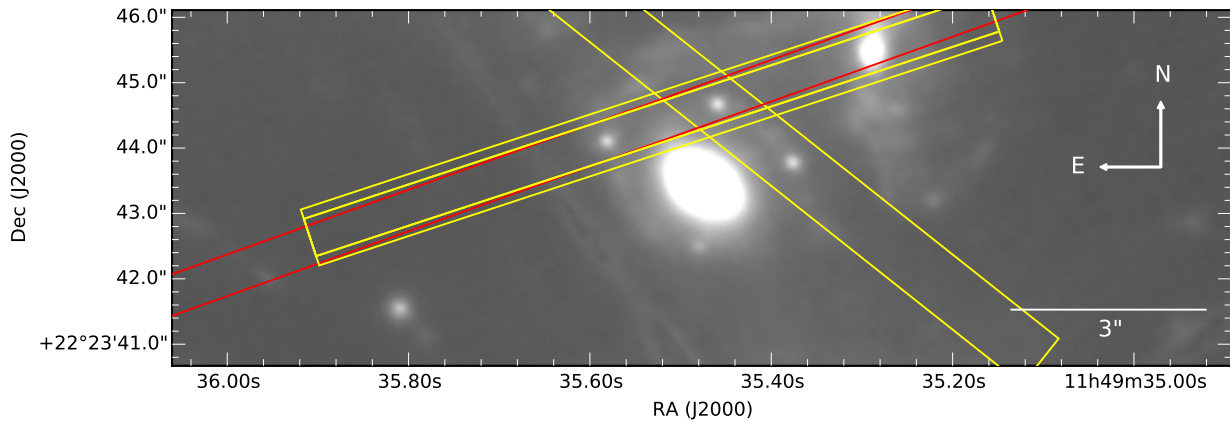

Figure 1. Image of the slit positions used for the MOSFIRE (red) and X-shooter (yellow) observations. The image is a coaddition of $F125W$ exposures which shows the four images forming the Einstein cross.

The extraction of the SN light curve from the *HST* imaging is described in a companion paper (Rodney et al. 2015).

2.5. *VLT X-shooter Spectra*

Observations were acquired with the X-shooter echelle spectrograph (Vernet et al. 2011) mounted on Unit Telescope 2 (UT2) of the VLT in three observation blocks (OBs) executed on May 16 (OB1), June 15 (OB2), and June 16 (OB3), 2015. X-shooter covers the entire spectral range 3100–25,000 Å by directing incoming light simultaneously to three arms with complementary wavelength coverage. The observations of SN Refsdal were taken in nodding mode where positions A and B were separated by 7″ along the slit.

The fraction of light from a well-centered point source that enters a spectrograph slit depends on the slit width and the FWHM of the PSF. From an *R*-band acquisition image, we can directly estimate the PSF FWHM through X-shooter at the beginning of each OB. The European Southern Observatory (ESO) Ambient Conditions Database[20] archives an estimate of the seeing at Cerro Paranal from the differential image motion monitor (DIMM). However, the DIMM seeing differs, in general, from the seeing achieved through X-shooter. The DIMM shows that conditions changed significantly during each of the three OBs.

In Table 3, we list estimates for the average seeing during each OB. We measure the seeing through X-shooter at the beginning of the OB from the FWHM of stars in the acquisition image. We then find the average FWHM recorded by the DIMM during the entire OB, and rescale this average value by the ratio between the DIMM FWHM at the start of the OB and the FWHM measured from the X-shooter acquisition image. The DIMM PSF measured a degradation from a FWHM of ∼ 0″.8 to ∼ 1″.6 and then settling at ∼ 1″.4 over the course of the OB1 observations. During the OB2 observation, the seeing gradually improved from ∼ 0″.75 to ∼ 0″.65. During the OB3 observation, the seeing evolved from ∼ 0″.7 to ∼ 0″.9 to ∼ 0″.8.

An overview of the observations is given in Table 2, and we show the slit positions in Figure 1. Observations of SN Refsdal were acquired at a high airmass almost orthogonal to the parallactic angle, so we need to consider carefully the effects of atmospheric dispersion (Filippenko 1982). The telescope tracks the target in images taken in 4700 Å, and a tip-tilt mirror corrects for the atmospheric refraction between 4700 Å and the middle of the atmospheric dispersion range for the NIR arm at 13,100 Å. Since the atmospheric dispersion in the NIR is comparatively small, X-shooter does not have an atmospheric dispersion corrector (ADC) to correct the NIR arm. The relative shift between 13,100 Å and Hα (∼ 16,330 Å) is expected to be only ∼ 0″.1. The relative atmospheric dispersion across the visible (VIS) arm is greater, and the ADC is not operational. We expect a ∼ 0″.5 shift at [O II] (∼ 9274 Å) relative to 4700 Å, the tracking wavelength where the target is centered on the slit. The slit width in the VIS spectroscopic arm is

0″.9 for OB1 and 1″.2 for OB2 and OB3. We test that the emission-line ratios in the NIR arm are not significantly affected by comparing spectra from OB1 and OB2 to OB3, for which the PA was closer to the parallactic angle.

3. PHOTOMETRIC CLASSIFICATION

During the first three months of observations after discovery on November 11, 2014, SN Refsdal continued to rise in brightness well beyond the time where any normal Type Ia, Ib, or Ic SN would have reached its peak luminosity (Kelly et al. 2015b). Continued monitoring showed that the light curve rose for ∼ 150 days, and the SN became similarly incompatible with most normal Type II SN light curves, which brighten to a "luminosity plateau" over only several days to weeks in the rest frame (Barbon et al. 1979; Doggett & Branch 1985). In Figure 4, we plot a comparison between the full SN light curves for S1–S4 against SN light-curve models for typical SNe Ia, SNe Ib/c, and SNe II.

This slow rise in brightness to a broad peak is consistent with the light curve of SN 1987A, a peculiar Type II SN in the Large Magellanic Cloud (LMC) that is the nearest and brightest SN observed in the last four centuries (Arnett et al. 1989, and references therein). SN 1987A brightened steadily in the rest-frame optical after initial emission from the shock breakout subsided to reach peak luminosity ∼ 84 days after first light; see Figure 3 from Filippenko (1997) for a comparison with SNe IIP. The progenitor of SN 1987A was identified as a blue supergiant (Sk −69°202; Gilmozzi et al. 1987; Sonneborn et al. 1987) in the LMC ($d \approx 50$ kpc), and more recent SNe with similar light-curve shapes and spectra are understood to be the result of the explosions of these compact massive stars. Well-studied examples of nearby SN 1987A-like events include SN 1998A (Pastorello et al. 2005), SN 2000cb and SN 2005ci (Kleiser et al. 2011), SN 2006V and SN 2006au (Taddia et al. 2012), and SN 2009E (Pastorello et al. 2012). These show a wide range of light-curve shapes and colors, explosion energies, and expansion velocities (e.g., Pastorello et al. 2012; Taddia et al. 2012).

However, one published example of a SN IIn, SN 2005cp (Kiewe et al. 2012), shows a light curve similar to that of SN 1987A. SNe IIn are characterized by relatively narrow H emission lines originating in the interaction between the expanding ejecta and pre-existing CSM. The interaction produces narrow Balmer emission and can power a strong underlying continuum. In Figure 5, we compare the $F160W$ (rest-frame ∼ *R*-band) light curves of the four SN Refsdal images with the *R*-band light curves of SN 1987A-like SNe (SN 2006V and NOOS-005, SN 1987A) and the Type IIn SN 2005c.

In Figure 6, we show that SN Refsdal has a $F125W - F160W$ (∼ $V - R$ in the rest frame of the SN) color comparable to those of nearby SN 1987A-like SNe. At an early phase, SN Refsdal has a $F105W - F125W$ (∼ $B - V$) color comparable to those of SN 2006V and SN 2006au, the bluest SN 1987A-like SNe, but near maximum brightness the color of SN Refsdal is blue in comparison to even SN 2006V and SN 2006au. At almost all epochs and in both colors, SN 2005cp is bluer than SN Refsdal. Here we have applied K-corrections to the extinction-corrected colors of the comparison sample (see
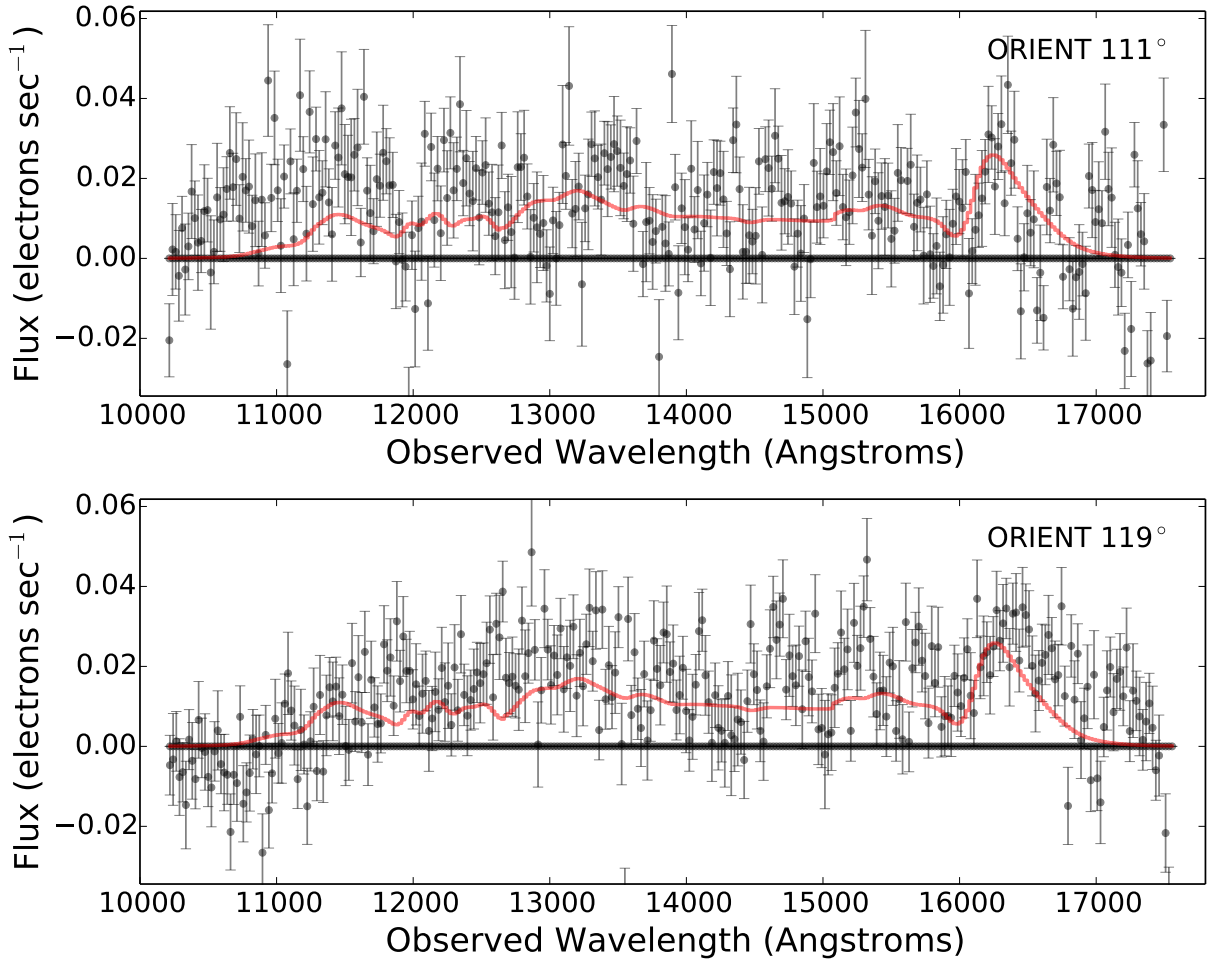
Figure 2. Spectra of image S2 extracted from grism data taken in the 111° and 119° *HST* orientations. The spectra taken in a pair of different orientations of the telescope, selected to minimize overlap with the traces of other objects, make it possible to obtain spectra that should contain different residuals from removal of overlapping traces. The superimposed spectrum of SN 1987A is normalized to the average $F160W$ magnitude of S2 during the period of observations.

Table 6). We apply no correction for possible dust extinction to the colors of SN Refsdal, since the low signal-to-noise ratio (S/N) or spectral resolution of the spectra do not allow any constraint on absorption by, for example, Na I D or diffuse interstellar bands.

For the sample of SN 1987A-like SNe included in Pastorello et al. (2012), the SNe show a range of absolute magnitudes (in the V, R, and I bands) from about -15 to -17.5 mag. In Figure 3, we show that SN Refsdal has a brighter M_B absolute magnitude and a bluer $B - V$ color near maximum light than the comparison sample of SN 1987A-like SNe. The magnifications predicted for sources S1, S2, and S3 are listed in Table 5. For a peak magnitude of $F160W \approx 24.25$ mag AB (see Rodney et al. 2015), SN Refsdal would have had an $M_R = -17.5$ mag (magnification $\mu = 25$) to $M_R = -18.5$ mag ($\mu = 10$). The range of possible absolute magnitudes imply that SN Refsdal would likely be the most luminous well-studied SN 1987A-like event.

In Figure 5, the broad-peaked shape of the light curve of OGLE-2003-NOOS-005[21] provides the best match to that of SN Refsdal. NOOS-005 was observed only in

[21] http://ogle.astrouw.edu.pl/ogle3/ews/NOOS/2003/noos.html

the I band and no spectrum was taken, so its color was not measured, but its I-band absolute magnitude ($M_I = -17.51$ mag) was the most luminous among those of SN 1987A-like SNe.

4. SPECTROSCOPIC CLASSIFICATION AND CHARACTERISTICS

The light curve and colors of SN Refsdal can be matched approximately by those of SN 1987A-like SNe II or, alternatively, SN 2005cp, a SN IIn. We next use the WFC3 grism and the VLT X-shooter spectra to confirm the Type II classification spectroscopically, and find evidence from the H features that strongly favors the identification of SN Refsdal as a SN 1987A-like SN instead of a SN IIn.

Figure 7 plots the binned WFC3 grism spectra of SN Refsdal taken in both the 111° and 119° telescope orientations. We plot the weighted average of the raw flux measurements (each 20 Å) within each 100 Å wavelength bin, and plot an uncertainty computed using bootstrapping with replacement. We show, for comparison, a spectrum of SN 1987A obtained at -41 days, of SN 1998A at -40 days (Pastorello et al. 2005), of SN 2006V at -25 days, and of SN 2006au at -19 days (Taddia et al. 2012).
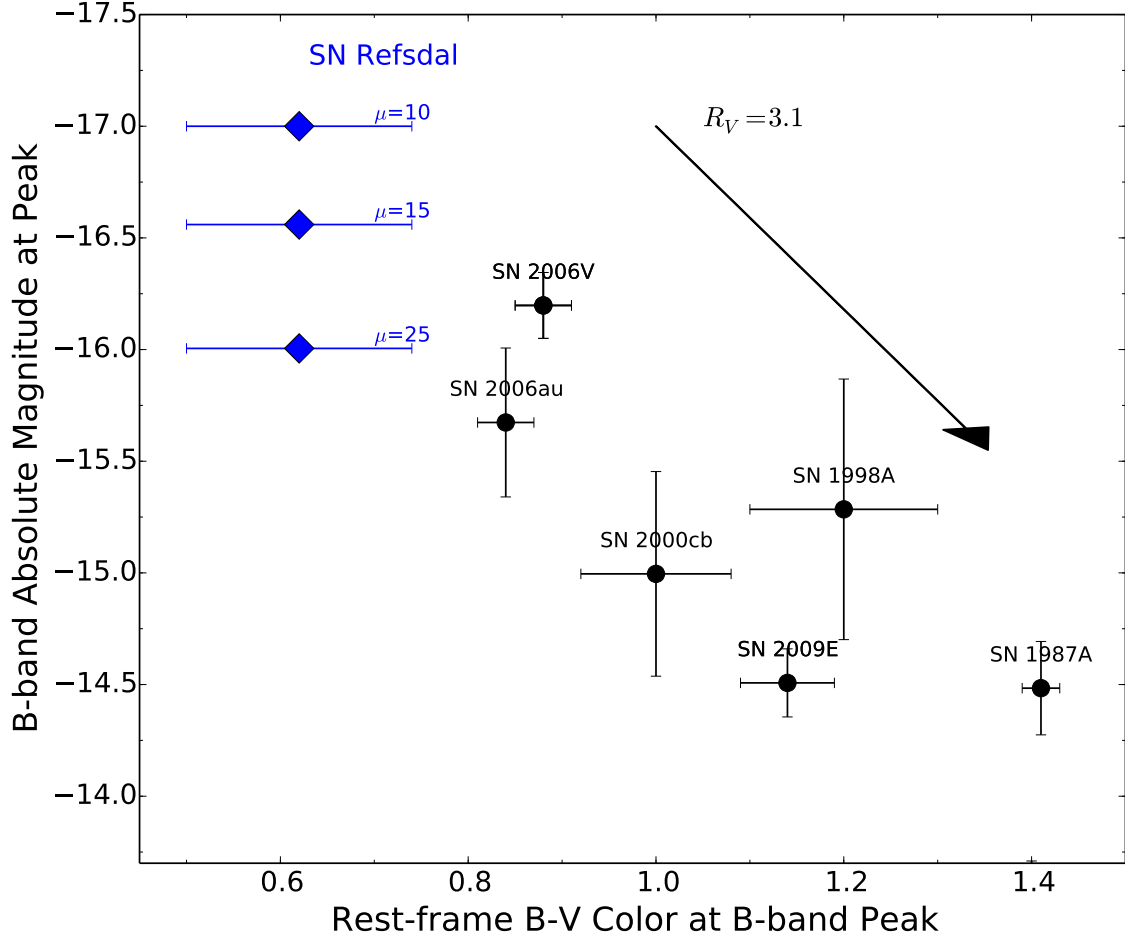
Figure 3. $B - V$ color and B-band absolute magnitude of SN Refsdal near light-curve peak in comparison to examples of low-redshift SN 1987A-like SNe. If a SN 1987A-like event, SN Refsdal would be the most blue ($B - V$, although not $V - R$) and potentially have the most luminous M_B absolute magnitude near the peak of its light curve, depending on the magnification. As seen in Figure 5, the slowly evolving light of SN Refsdal may be best matched by that of NOOS-005, which had the most luminous M_I absolute magnitude near peak but lacked photometry through other broadband filters or spectroscopy. The $B - V$ color and B-band luminosity of the SN 1987A-like SNe are corrected for reddening and extinction along the line of sight, but no correction is applied to the photometry of SN Refsdal. For illustration, we plot a reddening vector for $E(B - V) = 0.33$ mag for an $R_V = 3.1$ extinction law. Table 5 lists the magnifications of the images of the SN predicted by models of the galaxy and cluster lenses.

These spectra are scaled so that $F160W = 25.1$ mag AB, the average flux of the SN during the grism observations.

In Figures 8 and 9, we plot the spectral region near Hα for the WFC3 grism and X-shooter spectra. These exhibit broad Hα emission that spectroscopically classifies SN Refsdal as a Type II SN.

4.1. Hα P-Cygni Absorption

A strong and wide Hα P-Cygni absorption feature is present in the spectra SN 1987A-like SNe II but absent from the spectra of SNe IIn. In SN 1987A-like SNe II, the characteristic broad and deep P-Cygni absorption develops as the photosphere recedes into the ejecta. By contrast, the ejecta of SNe IIn collide with CSM and the photosphere generally forms in proximity to the heated, shocked material.

First, we smooth the SN spectrum using a $\sigma = 2000\,\mathrm{km\,s^{-1}}$ Gaussian kernel and variance weighting. After removing $> 5\sigma$ outliers from the data, we resmooth the spectrum with outliers removed using the same ker-

nel. We search the smoothed spectrum across the wavelength range 15,300–16,100 Å to find the absorption minimum.

To determine the uncertainty of the wavelength of the absorption minimum, we use boostrap resampling. For the grism and X-shooter spectra, we assemble the set of all flux measurements at each wavelength taken in both orientations or in all combinations of OBs and SN images, respectively. We resample these sets of measurements with replacement to create the full set of bootstrapped spectra.

The distribution of absorption minima we measure from the bootstrapped WFC3 grism spectra is approximately Gaussian. After rejecting a small population of $> 5\sigma$ outliers, we find an absorption minimum of $-8356\pm1105\,\mathrm{km\,s^{-1}}$ (15,880$\pm$60 Å). In contrast, the distribution of absorption minima we measure from the bootstrapped X-shooter spectra has a bimodal shape and is substantially broad, stretching over $\sim$ 15,650–16,050 Å. After removing a small number of outlying measurements
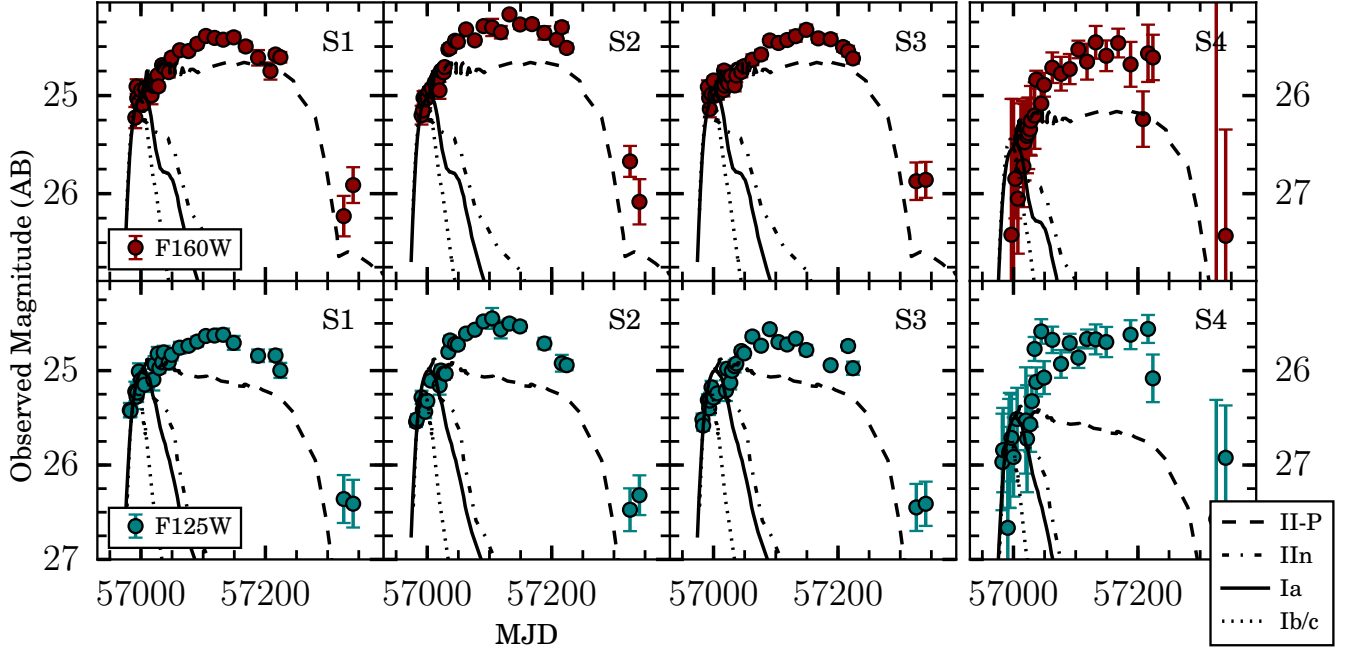
Figure 4. Four columns of panels show light curves of images S1–S4 of SN Refsdal from left to right. Top and bottom rows show the $F160W$ and $F125W$ photometry, respectively. The SN Ia and SN Ib/c templates are clearly incompatible with the broad light-curve shape of SN Refsdal, while normal SNe IIP ("plateau") do not show rising luminosities during their plateau phase.

close to 15,300 Å, we constrain the absorption minimum to be $-6465\pm2918\,\mathrm{km\,s^{-1}}$ (15,983±159 Å).

We next perform a data-driven simulation of the WFC3 grism spectrum to determine the statistical significance of finding the absorption feature we identify. As a first step, we smooth the grism spectrum using a $\sigma = 2000\,\mathrm{km\,s^{-1}}$ Gaussian kernel, and calculate the residuals of the data from the smoothed spectrum in the wavelength range 14,000–16,100 Å. Each simulated spectrum is created by replacing the flux at each wavelength in the grism spectrum with a randomly drawn value from the distribution of residuals.

With 10,000 simulated spectra, we compute a test statistic that measures the strength of the absorption relative to the continuum. To estimate the continuum level, we calculate median($f_{1.45-1.55}$), the median flux in the wavelength range 14,500–15,500 Å. We next calculate median($f_{\mathrm{absorp}}^{\mathrm{H\alpha}}$), the median flux within ±150 Å of the absorption minimum which corresponds to the 2–3σ width of SN 1987A-like SN II Hα absorption features (see Figure 8). The difference,

$$\Delta_{\mathrm{absorp}} = \mathrm{median}(f_{\mathrm{absorp}}^{\mathrm{H\alpha}}) - \mathrm{median}(f_{1.45-1.55}), \quad (1)$$

is used as the test statistic to compute a p value. For the grism spectrum, we measure $\Delta_{\mathrm{absorp}}^{\mathrm{grism}} = (-2.5 \pm 0.9) \times 10^{-20}\,\mathrm{erg\,s^{-1}\,cm^{-2}\,\AA^{-1}}$. We compute the probability of finding a lesser value $\Delta_{\mathrm{absorp}}^{\mathrm{grism}}$ by random chance using the spectra we simulate. We compute $p = 0.004$, which provides statistically significant evidence against the hypothesis that the apparent Hα absorption feature in the grism spectrum is a random artifact.

Given the width of the Hα absorption feature and $p = 0.004$ significance, we would not expect any other sim-

ilarly strong absorption feature, and none exists in the range 14,000–16,100 Å. If we instead extend the wavelength range used in the analysis blueward to 11,500–15,500 Å, then the p-value increases to ~ 0.02. Simulating grism spectra by repeatedly randomly drawing from residuals does not model any covariance in the random noise, although we do not expect a strong covariance.

In the case of the X-shooter spectra, the wavelength of the absorption minimum is poorly constrained, so it is not possible to apply the same statistical test. For the purpose of completeness, however, we calculate the p value for an absorption feature located at 15,983 Å, the median of the absorption minima measured from the bootstrapped spectra. The continuum is measured as the median of the spectrum regions 15,300–15,600 Å and 16,500–17,000 Å. We calculate $p = 0.800$ but note that 15,983 Å does not coincide with either peak of the bimodal distribution of minima measured from the bootstrapped spectra.

4.2. Hα Expansion Velocity Evolution and Comparison to SN 1987A-like SNe

In Figure 10, we plot the constraints on the Hα expansion velocity, and compare the measurements against the expansion velocities of SN 1987A, SN 2006V, and SN 2006au measured by Taddia et al. (2012). The grism measurement at -47 ± 8 d favors an Hα velocity comparable to that of the blue (see Figure 6) SN 1987A-like SN 2006V. The approximate X-shooter constraint on the expansion velocity at $+16 \pm 8$ d is consistent with the evolution of the Hα expansion velocity of SN 1987A-like events.

4.3. Models of the Hα Emission and Absorption Profiles
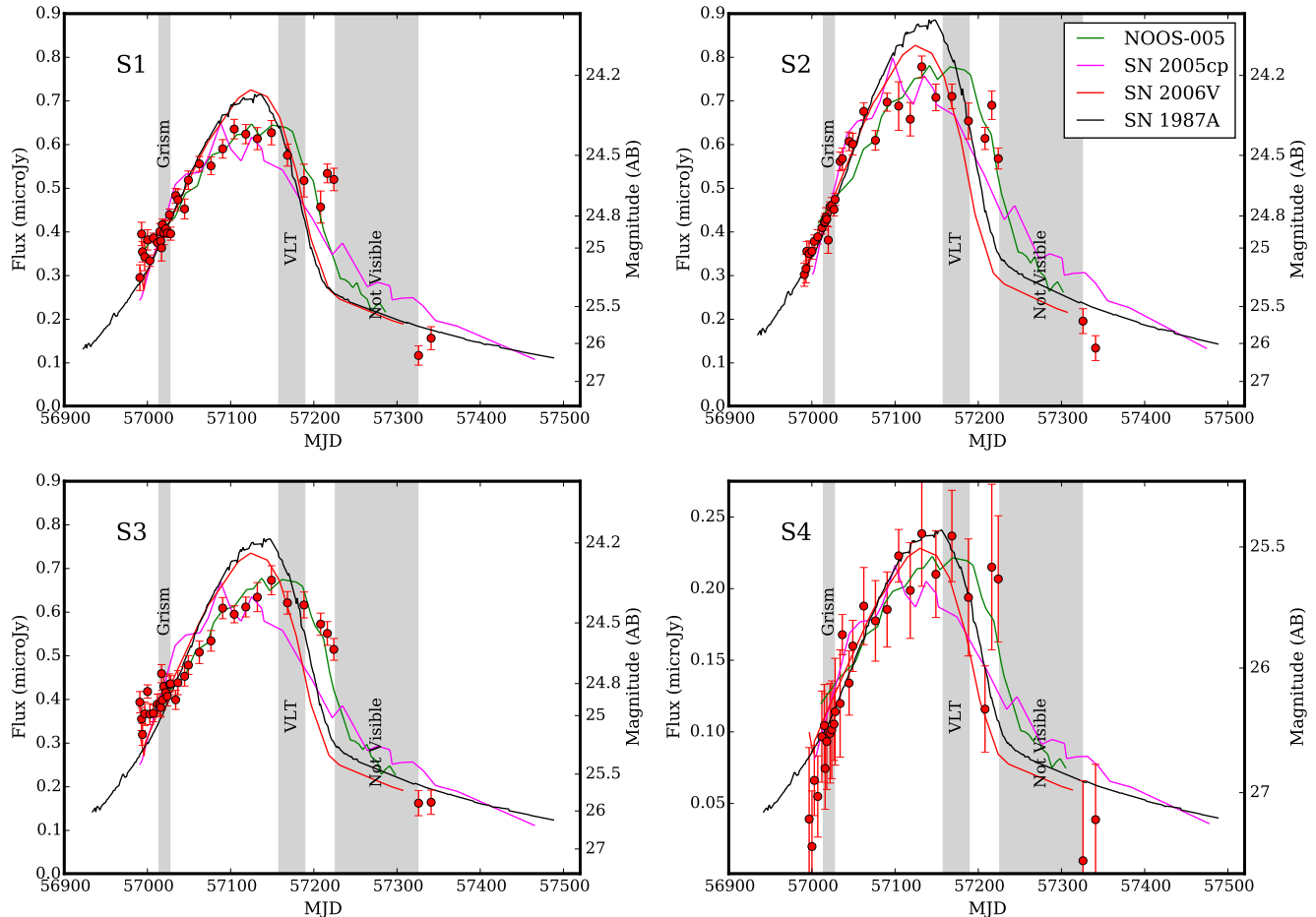
Figure 5. Comparison of SN Refsdal photometry to the light curves of SN 1987A-like SNe and the Type IIn SN 2005cp. NOOS-005 has the broadest peak and provides the best match to that of the SN Refsdal among examples of SNe with SN 1987A-like light curves. The color or spectroscopic properties of NOOS-005 are not known, because it was observed only through the I band, and it reached a luminous absolute magnitude. While SN 2005cp has a different spectroscopic classification which indicates the presence of significant CSM interaction, it may also be an explosion of a blue supergiant progenitor.

The Hα emission from SNe IIn generally exhibits a Lorentzian profile that arises from Thompson scattering of photons off of free electrons (Chugai 2001; Smith et al. 2010), while Doppler broadening of Hα emission from SN 1987A-like SNe instead produces approximately Gaussian profiles. Since the line shape contains information about the SN spectroscopic type, we examine which functional form better fits the grism and X-shooter spectra. As shown in Figures 8 and 9, we also model the grism spectrum with a P-Cygni profile including an absorption feature.

The model fits provide strong evidence favoring a Gaussian profile over a Lorentzian profile, and very strong evidence for a P-Cygni model for the WFC3 grism spectrum. In Table 4, we list the differences in the Akaike information criterion (AIC; Akaike 1974) to interpret the differences in the χ^2 statistics. A change of 2 in the AIC provides evidence against the model having a greater AIC value, while a difference of 6 constitutes strong evidence (e.g., Kass & Raftery 1995; Mukherjee et al. 1998). The AIC penalizes models having a greater number of parameters. A Gaussian model for the absorption feature in the grism spectrum yields a $\sim 4300\,\mathrm{km\,s^{-1}}$ FWHM.

4.4. Measurements of the Hα Line Profile and Flux

In Figure 11, we compare the total Hα luminosity of SN Refsdal at $-47\pm8\,\mathrm{d}$ and $+16\pm8\,\mathrm{d}$ with the Hα luminosity of SN 1987A-like SNe, as well as SN 2005cp. The strength and change in the Hα emission are consistent with the characteristics of Hα emission from SN 1987A-like SNe. We adopt a magnification of $\mu = 15$ to estimate the absolute luminosity, and error bars correspond to a 50% uncertainty in the magnification (see Table 5).

4.4.1. Comparison with Spectra of Other Supernovae

In Figures 12 and 13, we compare the grism and X-shooter data with spectra of SN 1987A-like SNe as well as SN 2005cp at a similar phase. For each comparison spectrum, we also calculate the χ^2 agreement with the spectrum of SN Refsdal in the wavelength range 15,000–17,000 Å.

To perform a comparison, we scale the spectrum of the low-redshift SN so that its synthetic $F160W$ flux matches the average flux of SN Refsdal when it was observed. While we have already subtracted the galaxy contribution from the grism spectrum at an earlier step, we need to model the underlying galaxy light in the X-shooter spectrum. We use the spectrum of an Sc galaxy

Table 4
Akaike Information Criteria

| | *HST* WFC3 Grism | | VLT X-shooter | |
Model	ΔAIC	χ^2	ΔAIC	χ^2
Lorentzian	0.0	185.8 ($N_{\mathrm{param}} =3$)	0.0	7223.8 ($N_{\mathrm{param}} =5$)
Gaussian	-4.8	181.0 ($N_{\mathrm{param}} =3$)	-17.3	7206.5 ($N_{\mathrm{param}} =5$)
P Cygni	-12.4	167.4 ($N_{\mathrm{param}} =6$)	...	...

Note. — Increments in the AIC for models of the Hα emission and absorption. A difference greater than 6 is considered strong positive evidence against the model with the higher value. We do not calculate a P-Cygni model for the VLT X-shooter spectrum, because we are only able to constrain the value of the minimum approximately. A Gaussian profile is favored over a Lorentzian profile for both the WFC3 grism and the X-shooter grism data, and a P-Cygni absorption feature is very strongly favored for the WFC3 grism spectrum.
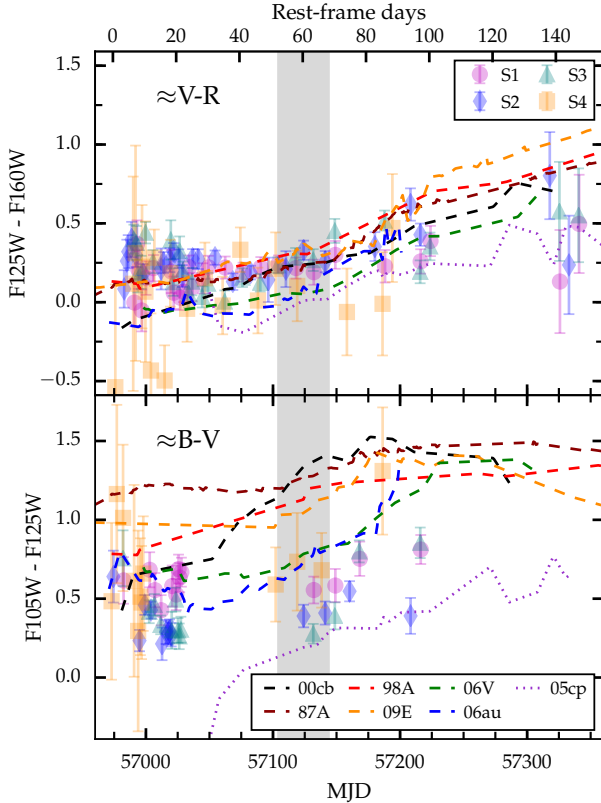
Figure 6. Comparison of the $F105W - F125W$ and $F125W - F160W$ colors of SN Refsdal with those of SN 1987A-like SNe as well as the Type IIn SN 2005cp as a function of phase relative to maximum light. At all phases for which we have photometry, SN Refsdal shows a $F125W - F160W$ ($\sim V - R$) color consistent with those of SN 1987A-like SNe. At an early phase, SN Refsdal exhibits a $F105W - F125W$ ($\sim B - V$) color that may be comparable to those of SN 2006V and SN 2006au, the bluest known example of a SN 1987A-like event. Near maximum light, SN Refsdal may be $B - V \approx 0.1$–0.2 mag bluer than SN 2006V and SN 2006au. The $B - V$ color of SN 2005cp, a SN IIn whose light curve resembles that of SN 1987A, is bluer than that of SN Refsdal at all phases having photometry.

Table 5
Predicted Magnifications

Model	μ_{S1}	μ_{S2}	μ_{S3}
Kelly et al. (2015b)	~ 10	~ 10	~ 10
Oguri (2015)	15.30	17.66	18.29
Sharon & Johnson (2015)	$18.5^{+6.4}_{-4.5}$	$14.4^{+7.5}_{-5.5}$	$20.5^{+19.1}_{-3.9}$
Grillo et al. (2015) (G12F)	$16.0^{+1.4}_{-5.7}$	$14.3^{+4.5}_{-6.4}$	$15.2^{+4.0}_{-4.9}$
Jauzac et al. (2015)	22.4 ± 2.0	18.9 ± 2.3	19.7 ± 1.7

Note. — Magnifications of images S1–S3 (for which we have spectra) predicted by models of the combined gravitational potential of the early-type galaxy and the MACS1149 galaxy cluster lenses.

4.5. *Constraint on the Supernova Ejecta Mass*

Following Taddia et al. (2012), we scale the parameters of the Blinnikov et al. (2000) model of SN 1987A to estimate the ejecta mass of SN Refsdal. To scale the model, we use the relation $t_d \approx (\kappa M_{\mathrm{ej}}/v)^{1/2}$ from Arnett (1979), where t_d is the diffusion time, κ is the mean opacity, and v corresponds to the expansion velocity. We lack direct constraints on the explosion date and the time of the bolometric peak, but SN 1987A-like SNe exhibit a small dispersion in their rise times; see Table 5 of Pastorello et al. (2012). These assumptions and a scaling according to the Hα expansion velocity yield an estimate for the ejecta mass of 20 ± 5 M$_\odot$.

4.6. **Superfit** *Analysis of Grism Spectrum*

To identify the spectroscopic classification of a SN, the **Superfit** (Howell et al. 2005) tool computes the χ^2 agreement between an input spectrum and a set of template SN spectra[22] reddened (or dereddened) by a range of A_V values. If the redshift of the SN is uncertain, template spectra can also be shifted across the possible redshifts of the SN. To calculate the χ^2 statistic, **Superfit** can use the uncertainties of the values in the spectrum.

We apply **Superfit** to find the SN that best matches the grism spectrum of SN Refsdal. Given the similarity of the light curve of SN Refsdal to those of SN 1987A-like SNe, we add spectra of SN 1998A, SN 2005cp, SN 2006V, SN 2006au, and SN 2009E to the set of **Superfit** template spectra. Since the position of the lensed source is near the tip of a spiral arm of a lensed galaxy, we fix the SN redshift to that of the host ($z = 1.49$) to investigate whether we can obtain a satisfactory fit. We allow the extinction A_V to vary between -2 and $+2$ mag, and we do not include any contribution from the host galaxy

redshifted to $z = 1.49$ (spiral host galaxy) as a model the galaxy light, and vary its normalization to find the best match to the data. Using the spectrum of an S0 galaxy at $z = 0.54$ (early-type galaxy lens) yields almost identical results. All of the low-redshift comparison spectra are corrected for the Milky-Way and host-galaxy extinction values listed in Table 6.

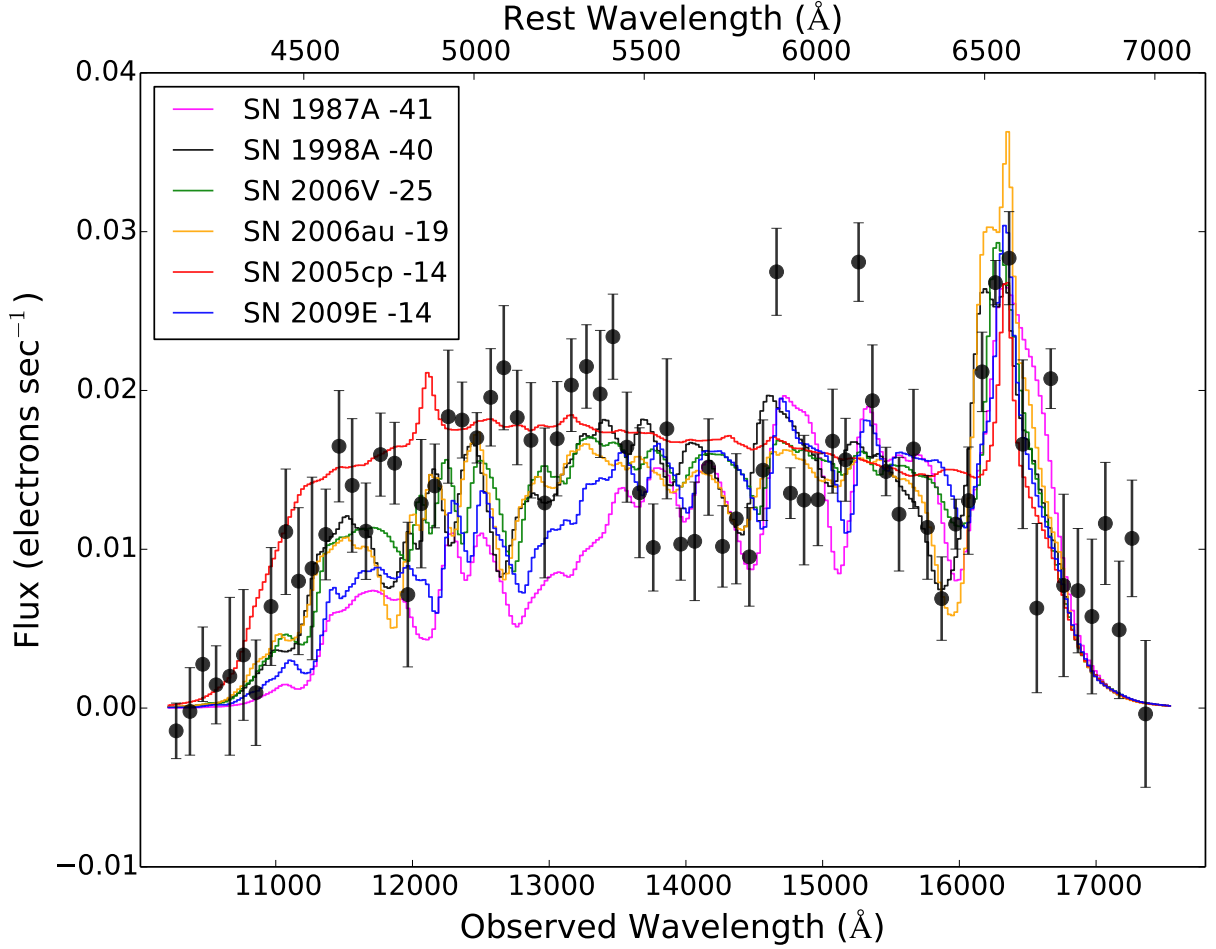[22] https://github.com/dahowell/superfit

Figure 7. Combination of grism spectra taken in both 111° and 119° orientations and binned in wavelength. Each bin is 100 Å in width, and plotted uncertainties are estimated through bootstrapping with replacement fluxes in the 20 Å bins. The grism spectra contributing to this combined spectrum have phases of -47 ± 8 d days. SN Refsdal exhibits stronger Hα emission and a bluer continuum at this phase. The color of the SN measured from coadded direct images taken after each grism integration shows agreement with that computed from synthetic magnitudes.

Table 6
Nearby Supernovae with SN 1987A-like Light Curves

SN	Host $E(B-V)$ (mag)	Milky Way $E(B-V)$ (mag)	D (Mpc)	R- or r-band Max. (MJD)	Spectroscopy Dataset	Photometry Dataset
SN 1987A	0.13 (1)	0.06 (2)	0.50±0.005	46933.10±1.0	3	4
SN 1998A	~ 0 (5)	0.12	33±10	50885.10±3.9	5	6
SN 2005cp	0.02 (6)	0.03	120±9.9	53581	7,8	7
SN 2006V	~ 0 (7)	0.029	72.7±5	53824.23	9	9
SN 2006au	0.141 (8)	0.172	46.2±3.2	53866.25	10	10
SN 2009E	0.02 (8)	0.02	29.97±2.10 (8)	54927.8±2.8	10	10

Note. — Publications containing data used for comparison. Many of the spectra were retrieved from WISEREP[a] (Yaron & Gal-Yam 2012). Welty et al. 2012 (1); Staveley-Smith et al. 2003 (2); Hamuy & Suntzeff 1990 (3); Phillips et al. 1988[b] (4); Phillips et al. 1990[c] (5); Pastorello et al. 2005 (6); Kiewe et al. 2012 (7); Silverman et al. 2012 (8); Taddia et al. 2012 (9); Pastorello et al. 2012 (10). Distances taken from NASA/IPAC Extragalactic Database[d] except if another citation is provided. Milky Way extinction from Schlafly & Finkbeiner (2011), except for the case of SN 1987A in the LMC.
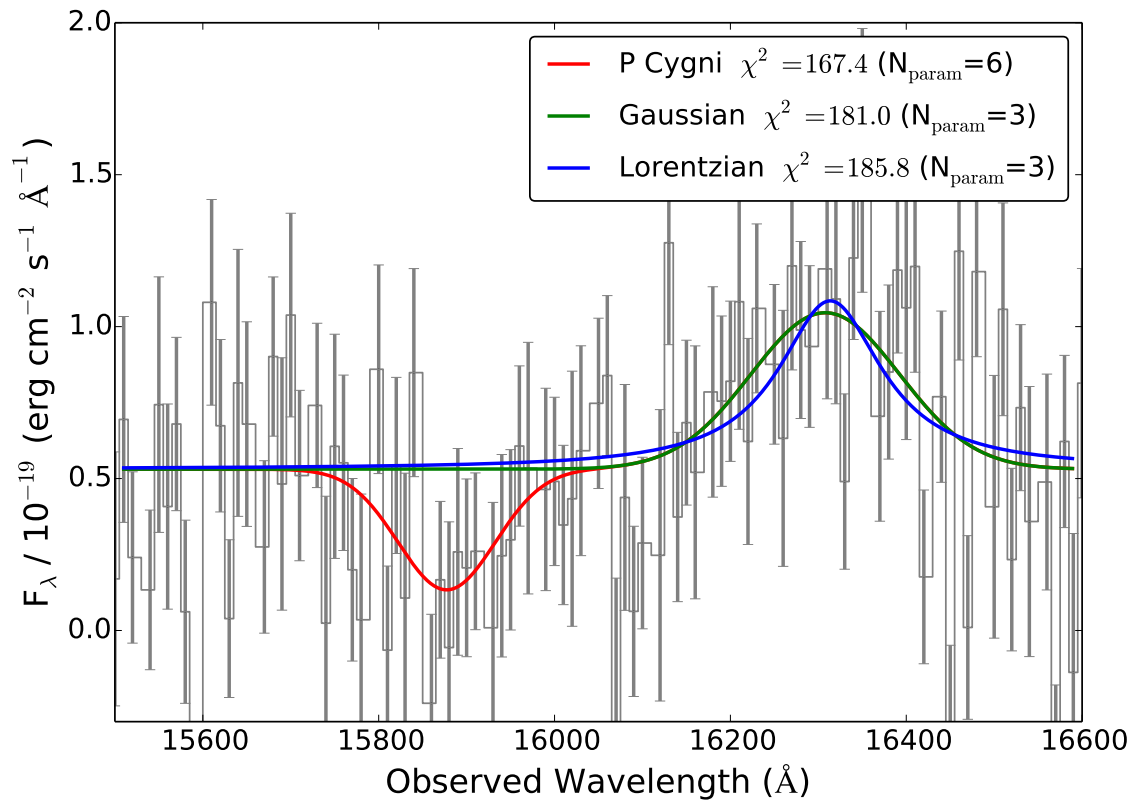
[a]http://wiserep.weizmann.ac.il/
[b]http://www.physics.unlv.edu/jeffery/astro/sne/spectra/d1980/sn1987a/old/
[c]ftp://ftp.noao.edu/sn1987a
[d]https://ned.ipac.caltech.edu/

Figure 8. Model fits to *HST* WFC3 G141 grism spectrum of Hα taken $-47 \pm 8\,\mathrm{d}$ relative to maximum light. Table 4 lists the changes in the AIC between the model fits. While the χ^2 values listed are from fitting the unbinned spectra, we plot the spectra after binning above.
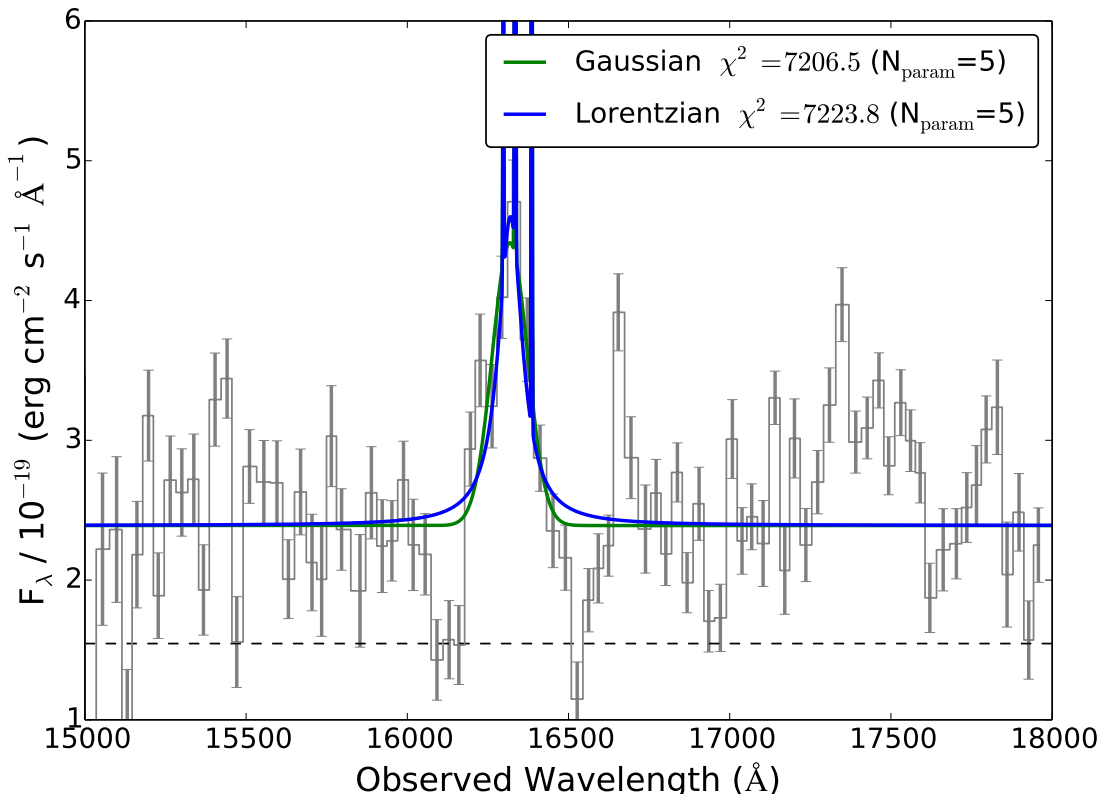
Figure 9. Model fits to the VLT X-shooter spectrum of Hα taken $+16 \pm 8\,\mathrm{d}$ relative to maximum light at the position of SN Refsdal. Table 4 lists the changes in the AIC between the model fits. While the χ^2 values listed are from fitting the unbinned spectra, we plot the spectra after binning above.

Table 7
Best-Fitting Template Spectra in Superfit Library

Supernova	Type	Phase	A_V (mag)	S
SN 1998A	II	-40	1.1	44.62
SN 2005cs	II	+2	1.9	48.98
SN 2005cs	II	+14	0.9	49.05
SN 2004et	II	+47	-0.9	49.20
SN 1999em	II	+20	-0.2	49.45
SN 1986I	II	+83	1.1	49.70
SN 2004et	II	+45	-0.7	49.79
SN 2005cs	II	+1	1.9	49.90
SN 2005cs	II	+6	0.9	49.98
SN 2005cs	II	+11	0.5	50.45
SN 1999em	II	+9	-0.2	50.48
SN 1999em	II	+15	-0.4	50.50
SN 1999em	II	+4	1.7	50.79
theory99em	II	+25	-0.7	50.85
SN 1993W	II	+21	-0.1	50.85

Note. — The fifteen best-matching `Superfit` (Howell et al. 2005) templates are SNe II showing P-Cygni profiles, which are characterized by the presence of H features. $S = \Sigma(F_i - T_i \times 10^{-A_\lambda/2.5})/\sigma_i^2$, where F_i is the F_λ flux of the SN measured in each resolution element, σ_i is the uncertainty of the measured flux, T_i is the flux of template spectrum, and A_λ is the wavelength-dependent extinction for an $R_V = 3.1$ law. The normalization of the template spectrum and the extinction A_V are the fitting parameters. We fix the redshift to be that of the host galaxy ($z = 1.49$).

since that has already been subtracted. Our input spectrum is not binned and includes the flux measurements taken in both telescope orientations, as well as the uncertainties in the measured fluxes. We adopt five iterations of 5σ outlier rejection, which is less aggressive than the default 2.7σ rejection.

Table 7 lists the fifteen best-fitting template matches to the grism spectrum in the wavelength range 14,000–16,750 Å. These include only SNe II having Hα P-Cygni profiles. If we extend the wavelength range to 11,000–16,750 Å, then a spectrum of SN 2005cp taken ~ 30–50 days after maximum light provides the fifth-best match. All other matches are SNe II having P-Cygni profiles. While the template spectrum of SN 2005cp was taken ~ 30–50 days after maximum light, the grism spectra of SN Refsdal were acquired at $-47 \pm 8\,\mathrm{d}$, and the Hα profile of SN 2005cp broadened significantly after maximum light as CSM interaction increased (see Figure 9 of Kiewe et al. 2012). As shown in Figure 11, the Hα evolution of SN Refsdal does not appear to be the same as that of SN 2005cp.

5. THE SN HOST GALAXY AND ENVIRONMENT

Since the progenitor of SN 1987A was identified as a blue supergiant star (Gilmozzi et al. 1987; Sonneborn et al. 1987), the precursors of SN 1987A-like SNe are believed to be similar — compact, short-lived, massive stars. The properties of the emitting gas near the explosion site of SN Refsdal measured from strong nebular lines should be similar to the properties of the gas that formed the massive progenitor of SN Refsdal. To mea-
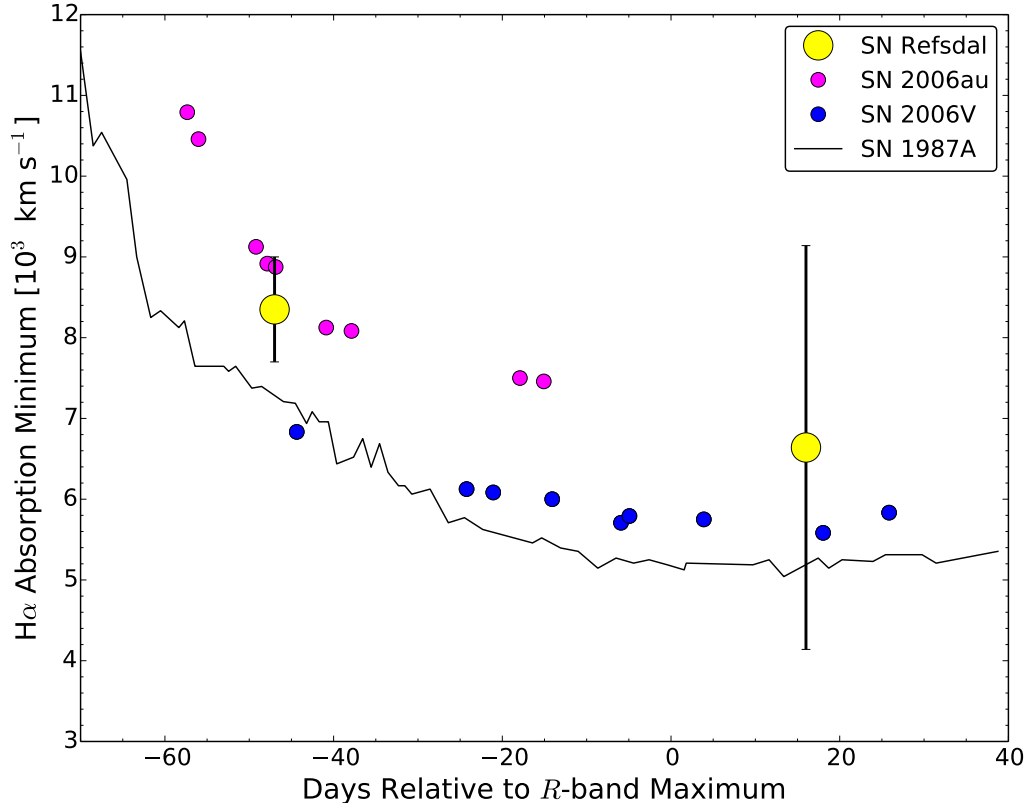
Figure 10. Comparison between constraints on Hα P-Cygni absorption expansion velocity and Hα expansion velocities of SN 1987A-like SNe. The plotted measurements of SN 2006V, SN 2006au, and SN 1987A are from Taddia et al. (2012). The early-time Hα expansion velocity of SN Refsdal is from the WFC3 grism spectra, and the later constraint is from the X-shooter spectra.

sure the host-galaxy narrow-line emission, we reduce the spectra in "stare mode" where we do not subtract the off-target spectra. This allows us to avoid subtracting any narrow-line emission from sources in the off-target position which can have bright emission lines. We list the narrow-line measurements in Tables 8 and 9 and the inferred extinction and properties of the ionized gas in Table 10.

As Figure 14 shows, we detect strong nebular emission both near the SN explosion site and from the nuclear region of the host galaxy. The emission from the nuclear region has a significantly broader profile, which we attribute to the rotational motion of the gas. From the best-fit line centers, we measure redshifts of 1.48831 ± 0.00007 from the spectrum extracted around the SN position and 1.48837 ± 0.00007 for the nuclear region, where the uncertainties include contributions from both line fitting and the wavelength solution.

To constrain the source of the ionizing radiation and properties of the emitting gas, we construct a Baldwin, Phillips, & Terlevich (BPT; Baldwin et al. 1981) diagram, plotted in Figure 15. The intensity ratios [O III]λ5007/Hβ and [N II]λ6584/Hα of the strong emission lines from near the SN site and the nuclear region are consistent with the ratios expected for gas ionized by radiation from massive stars, and the positions on the BPT diagram coincide with the Sloan Digital Sky Survey (SDSS; Thomas et al. 2013) star-forming galaxy population.

We next estimate the reddening along the line of sight

to the emitting gas from the measured Balmer decrement. Making the assumption of Case B recombination, we apply the prescription from Domínguez et al. (2013) and adopt the $R_V = 2.51$ Reddy et al. (2015) extinction curve inferred from MOSFIRE Deep Evolution Field (MOSDEF) spectroscopy of galaxies at $z \approx 1.4$–2.6. We estimate a color excess of $E(B-V) = 0.1 \pm 0.2$ mag ($A_V = 0.3 \pm 0.4$ mag) for the nuclear region and $E(B-V) = 0.8 \pm 0.4$ mag ($A_V = 2.0 \pm 1.0$ mag) near the SN site. In Table 10, we also list the extinction expected for Hα.

SN Refsdal occurred at an offset from its host galaxy's nucleus of ~ 7 kpc, and Yuan et al. (2015) used OSIRIS (Larkin et al. 2006) integral-field-unit observations to constrain the oxygen abundance from ~ 5–7 kpc to be $12 + \log(O/H)_{PP04N2} \leq 8.11$ dex by comparing an upper limit on the [N II] emission to the measured Hα flux using the Pettini & Pagel (2004) abundance diagnostic. As in Yuan et al. (2015), we use the Pettini & Pagel (2004) N2 metallicity indicator based on the ratio [N II] λ6584/Hα. We find that the nuclear region has an oxygen abundance of $12 + \log(O/H) = 8.6 \pm 0.1$ dex. From an upper limit on the [N II] flux, we compute a 3σ upper limit of 8.4 dex near the SN site. The MOSFIRE spectrum yields a 3σ detection of [N II] and an estimate for the oxygen abundance of $12 + \log(O/H) = 8.3 \pm 0.1$ dex. The presence of strong night-sky lines close to both [N II] emission lines limit the sensitivity of the spectra to the metallicity. Since the ratio of nitrogen to oxygen and the ionization parameter substantially affect the N2
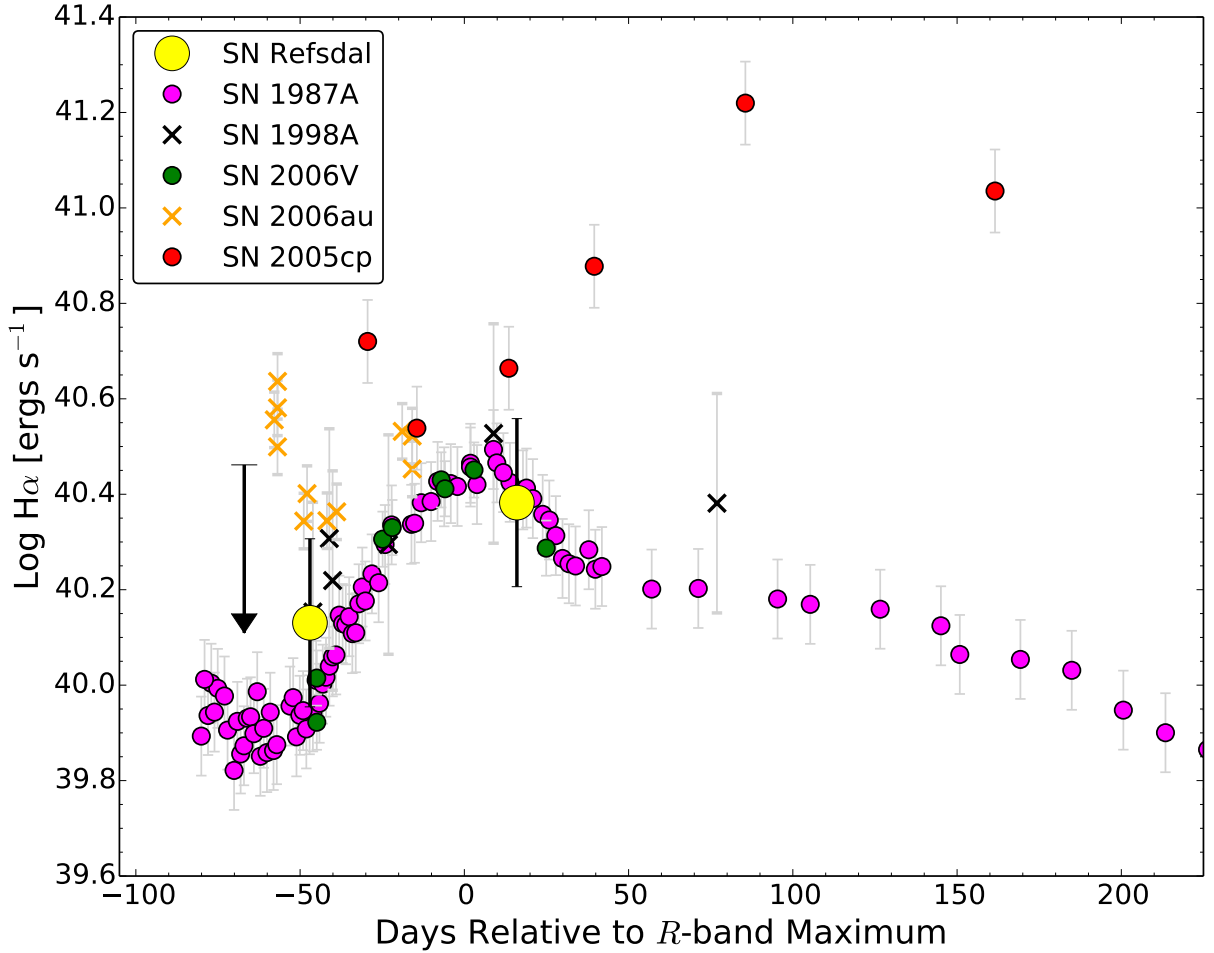
Figure 11. Comparison between the Hα luminosity evolution of SN Refsdal (after correcting for magnification) and that of SN with SN 1987A-like light curves. The SNe plotted for comparison were spectroscopically classified as Type IIP, with the exception of SN 2005cp. The relatively narrow Balmer emission lines of SN 2005cp led it to be classified as a SN IIn, although its light curve is similar to those of SN 1987A-like SNe. The upper limit on the Hα luminosity obtained -62 ± 8 d before R-band maximum is from the MOSFIRE integration, the measurement at -47 ± 8 d is from the WFC3 G141 grism data, and the measurement at $+16 \pm 8$ d is from the X-shooter spectrum. Plotted error bars correspond to uncertainties in the distance to the explosion, or in the case of SN Refsdal, magnification from the cluster.

Table 8
Keck-I MOSFIRE Host-Galaxy
Emission-Line Measurements

Line	Flux $(10^{-17}\,\mathrm{erg\,s^{-1}\,cm^{-2}})$
[N II] $\lambda6549$	0.197 ± 0.0598
Hα	5.87 ± 0.132
[N II] $\lambda6584$	0.592 ± 0.179
[S II] $\lambda6717$	1.34 ± 0.141
[S II] $\lambda6731$	0.854 ± 0.147

Note. — Measurements of emission lines and uncertainties. Fluxes are not corrected for extinction or magnification.
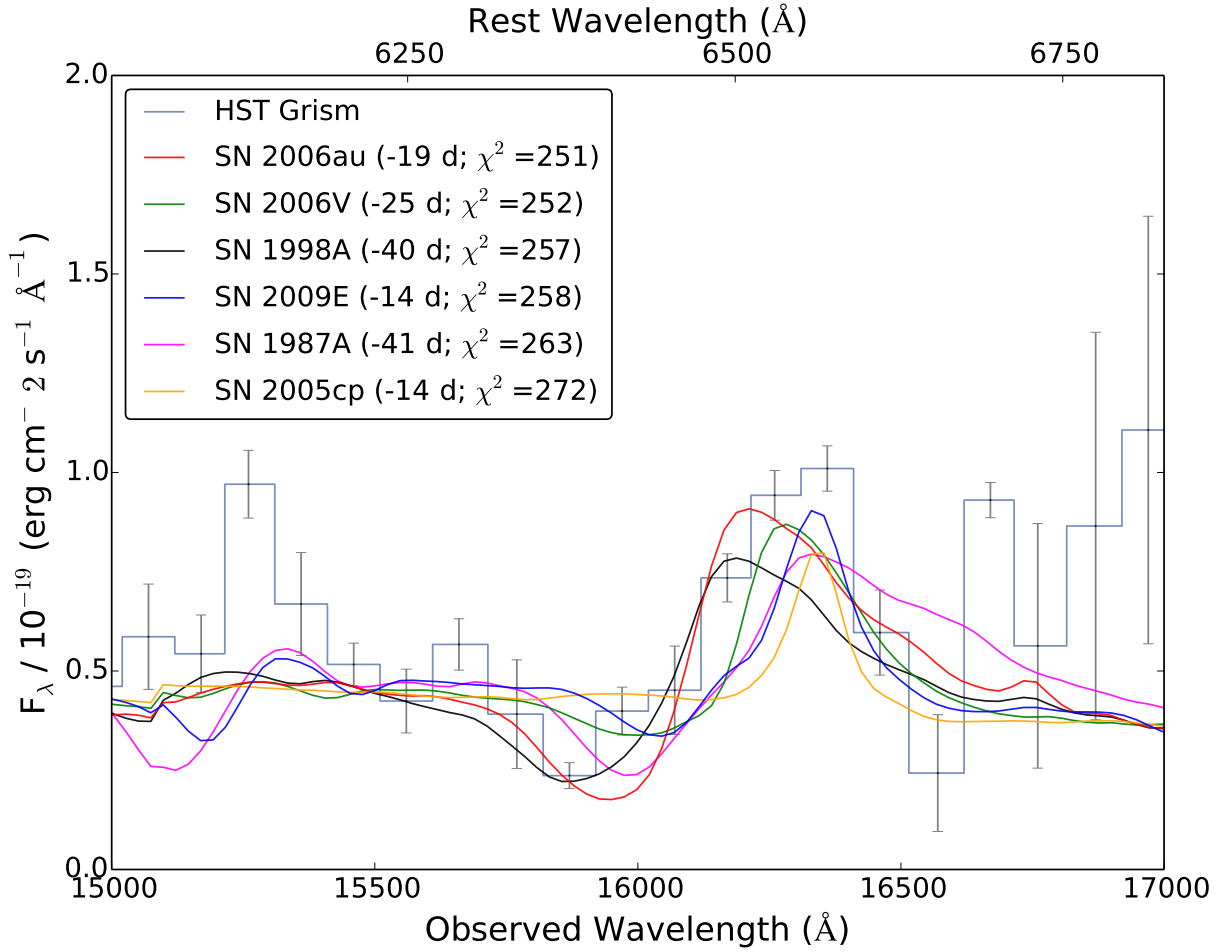
Figure 12. Comparison between the *HST* WFC3 G141 grism spectrum of Hα taken −47 ± 8 d relative to maximum light and the spectra of SN 1987A-like SNe taken at a roughly similar phase. Here we limit the comparison to a spectral region near the broad Hα. We have used a simulation of the grism to compute the expected spectrum, and these processed spectra are plotted. We compute the χ^2 agreement between the grism spectrum and the comparison spectra. Interpretation of χ^2 values on the basis of Kullback-Leibler information entropy (Akaike 1974; Sugiura 1978) indicates that a χ^2 difference of 2 is evidence against the more poorly fitting model and 6 constitutes strong positive evidence (e.g., Kass & Raftery 1995; Mukherjee et al. 1998). The grism data disfavor the relatively narrow Hα profiles of SN 2005cp, a SN 1987A-like SN that was classified as a SN IIn.
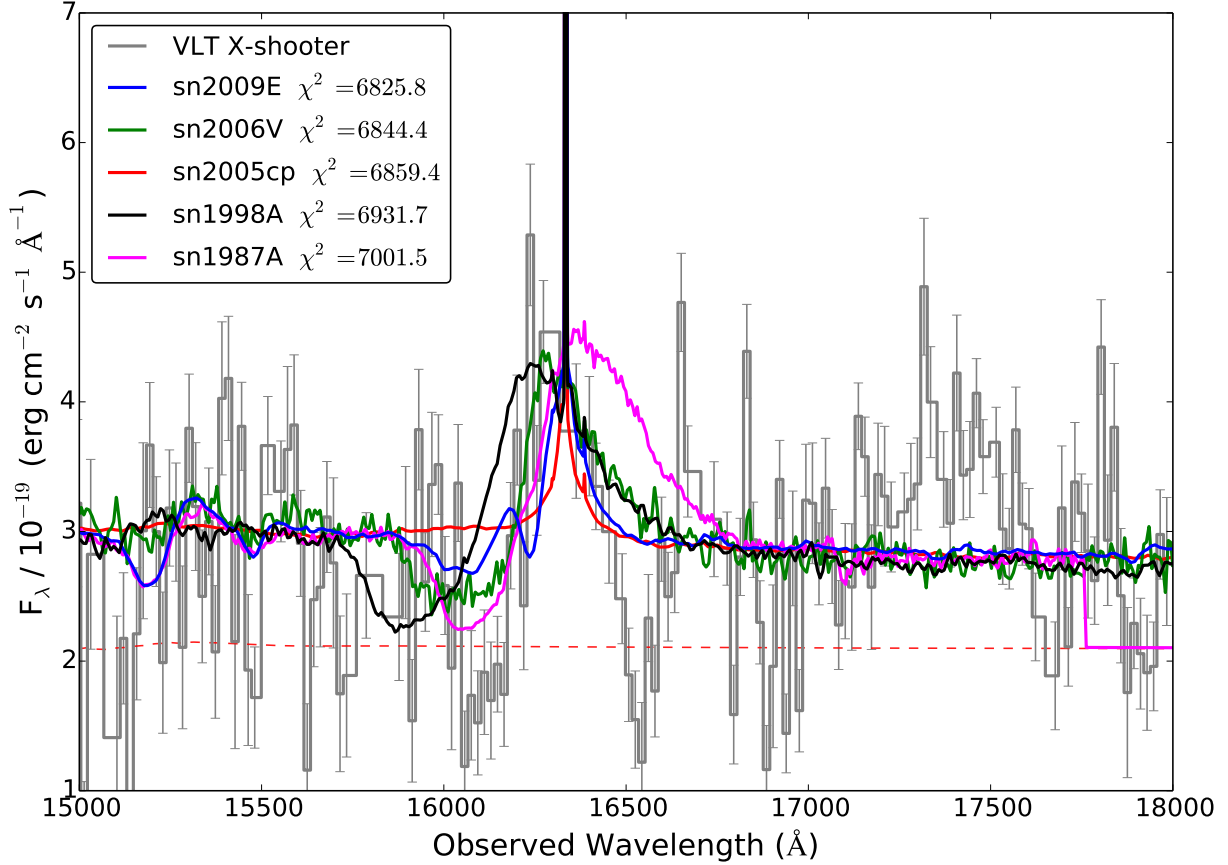
Figure 13. Comparison between the VLT X-shooter spectrum of Hα taken $+16 \pm 8$ d relative to maximum light and the spectra of SN 1987A-like SNe taken at a roughly similar phase. Here we limit the comparison to a spectral region near the broad Hα. We compute the χ^2 agreement between the X-shooter spectrum and the comparison spectra. Interpretation of χ^2 values on the basis of Kullback-Leibler information entropy (Akaike 1974; Sugiura 1978) indicates that a χ^2 difference of 2 is evidence against the more poorly fitting model and 6 constitutes strong positive evidence (e.g., Kass & Raftery 1995, Mukherjee et al. 1998). The VLT data disfavor the relatively narrow Hα profiles of SN 2005cp, a SN 1987A-like SN that was classified as a SN IIn.

Table 9
VLT X-shooter Host-Galaxy Emission-Line Measurements

Source	Line	Line Flux $(10^{-17}\,\mathrm{erg\,s^{-1}\,cm^{-2}})$	FWHM $(\mathrm{km\,s^{-1}})$
SN	[O II] λ3726	0.47 ± 0.08	43 ± 18
SN	[O II] λ3729	0.63 ± 0.01	-
SN	Hβ	0.2 ± 0.1	64 ± 16
SN	[O III] λ4959	0.25 ± 0.05	60 ± 14
SN	[O III] λ5007	0.7 ± 0.1	-
SN	Hα	1.5 ± 0.3	66 ± 11
SN	[N II] λ6584	≤ 0.24	62 ± 13
Host nucleus	[O II] λ3726	3.1 ± 0.2	185 ± 18
Host nucleus	[O II] λ3729	3.6 ± 0.2	-
Host nucleus	Hβ	4.4 ± 0.6	168 ± 7
Host nucleus	[O III] λ4959	0.9 ± 0.2	177 ± 20
Host nucleus	[O III] λ5007	1.0 ± 0.2	-
Host nucleus	Hα	14.0 ± 0.2	203 ± 30
Host nucleus	[N II] λ6584	4 ± 1	187 ± 18

Note. — Measurements of emission lines and uncertainties. Fluxes are not corrected for extinction or magnification. FWHM line widths are corrected for the instrumental resolution. For the instrumental resolution, the nominal value for the $0.''6$ slit is used since the FWHM of the PSF is comparable for all observations, so the resolution is set by the seeing rather than the slit width.
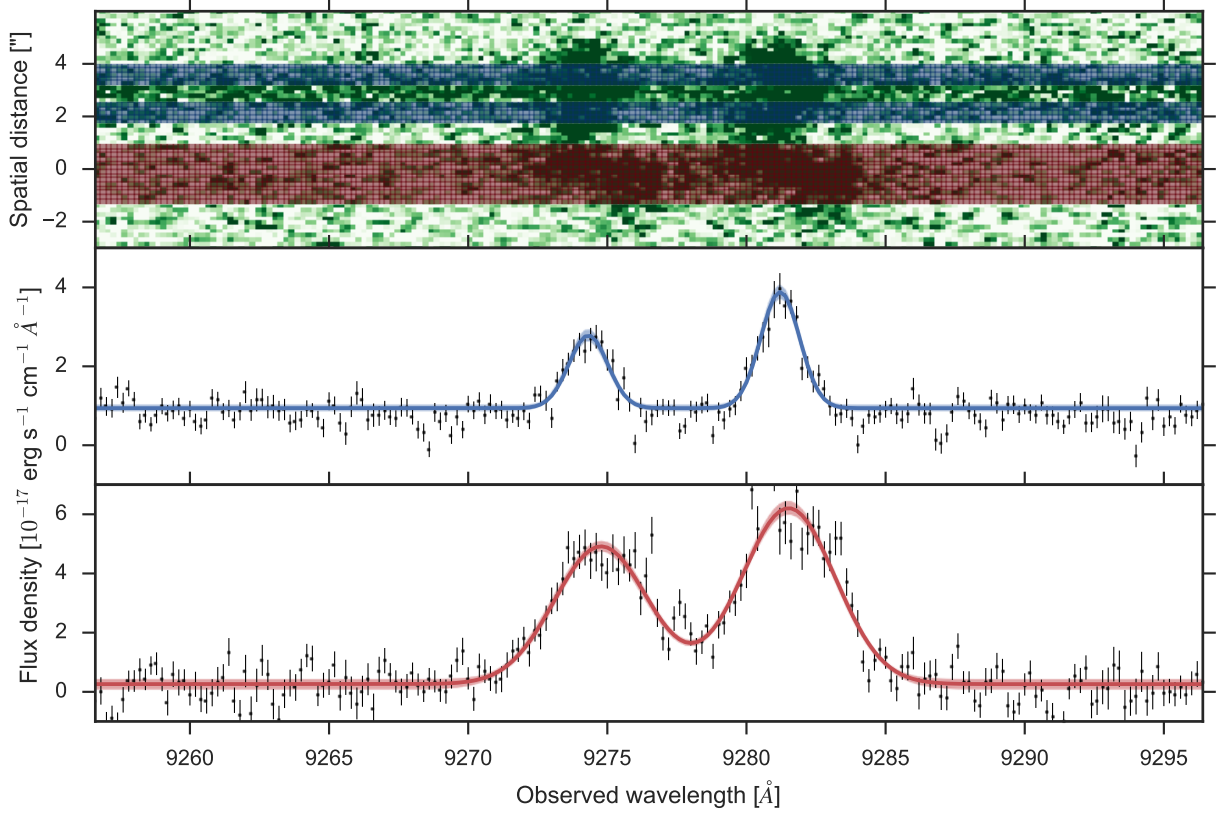
Figure 14. Example of nebular emission line detection in VLT/X-shooter spectra. The top panel is the two-dimensional spectrum from OB2 (see Figure 1) in the region surrounding [O II] $\lambda\lambda3726$, 3729. The ordinate corresponds to the spatial direction and the abscissa is the spectral direction. The blue-colored regions are the extraction apertures used for the position of the SN images S1 and S2 (above and below, respectively). The trace visible between the two SN positions is light from the early-type galaxy lens. The red-colored region is the aperture used to extract the spectrum of the host nucleus. The [O II] $\lambda\lambda3726$, 3729 doublet is cleanly resolved in the X-shooter spectrum, and significant structure is visible in both the spatial and dispersion directions. The middle panel shows the fit to the [O II] $\lambda\lambda3726$, 3729 emission lines at the SN positions, while the bottom panel plots the same for the host nucleus.

Table 10
Host-Galaxy Measurements

Measurement	Nuclear Region	SN Site	Instrument
$12 + \log(\text{O/H})$ (PP04 N2)	...	$8.3 \pm 0.1\,\text{dex}$	MOSFIRE
$12 + \log(\text{O/H})$ (PP04 N2)	8.6 ± 0.1 dex	$8.4\,\text{dex}$ (3σ upper limit)	X-shooter
$E(B-V)$	0.1 ± 0.2 mag	0.8 ± 0.4 mag	X-shooter
$A_{\text{H}\alpha}$	0.2 ± 0.3 mag	1.5 ± 0.9 mag	X-shooter
A_V	0.3 ± 0.4 mag	2.0 ± 1.0 mag	X-shooter

Note. — Properties of the ionized gas near the SN explosion site and in the host-galaxy nuclear region, as well as reddening along the line of sight from analysis of strong nebular emission lines.

metallicity diagnostic, our estimates may have an accuracy of only ~ 0.2 dex. The relatively large uncertainty in our measurement of Hβ implies that the R_{23} diagnostic (Pagel et al. 1979) is not able to provide a useful constraint on the oxygen abundance.

Karman et al. (2016) have used the Multi Unit Spectroscopic Explorer (MUSE) on the VLT to take optical spectra of the three separate images of the host-galaxy environment of SN Refsdal. Within a 0″.6-radius aperture surrounding the explosion site, they report a high ratio of [O II] to Mg II of 10–20, consistent with low metallicity and a high ionization parameter. From the X-shooter spectra, we measure 3σ limits on the flux of Mg II $\lambda 2796$ to be $\leq 4.7 \times 10^{-18}$ erg s^{-1} cm^{-2} and of Mg II $\lambda 2803$ to be $\leq 6.3 \times 10^{-18}$ erg s^{-1} cm^{-2}, which are consistent with the flux levels measured by Karman et al. (2016).

5.1. *Comparison of Host-Galaxy Environments*

The low oxygen abundance inferred for the explosion environment of SN Refsdal is consistent with a preference for low metallicity among low-redshift SN 1987A-like SNe. Taddia et al. (2013) found an average value of $12 + \log(\mathrm{O/H}) = 8.36 \pm 0.05$ dex (PP04 N2) for the local environments of SN 1987A-like SNe. They found that these abundances were more metal-poor than those of SN IIP environments (within ~ 3 kpc) measured by Anderson et al. (2010). Additional circumstantial evidence for low-metallicity environments include a preference for low-mass dwarf host galaxies, or the periphery of late-type spirals (Pastorello et al. 2012). By contrast, normal SNe II trace the light g-band light of their host galaxies (Kelly et al. 2008) and show no preference for metal-poor galaxies or the peripheries of their host galaxies (Kelly & Kirshner 2012).

6. SUMMARY

We have used *HST* WFC3 grism and VLT X-shooter NIR spectra and images to classify SN Refsdal, the first example of a resolved, strongly lensed SN. Its slowly rising broadband *HST* light curve can be matched by those of SN 1987A-like SNe, a peculiar class of SNe II that may account for ~ 1.5–3% of nearby SNe (Smartt et al. 2009a; Kleiser et al. 2011; Pastorello et al. 2012). The only other SNe having similar light curves and colors are SNe IIn, which erupt into dense CSM and whose light curves are heterogeneous. Detection of strong and wide Hα P-Cygni absorption in the grism spectrum, however, identifies SN Refsdal as a SN 1987A-like SN, and excludes the possibility that it is a SN IIn with continuum emission arising primarily from circumstellar interaction.

The specific properties of the Hα emission and absorption features are also consistent with measurements of low-redshift SN 1987A-like SNe. The Hα expansion velocity we measure from the grism spectrum agrees with the velocities of SN 1987A-like SNe at similar premaximum phases. Similarly, the strength and evolution of the Hα luminosity are consistent with those of SN 1987A-like events, and may not have been as strong or evolved the same way as was observed for the Type IIn SN 2005cp. Finally, the Hα emission-line profile is Gaussian instead of Lorentzian.

SN 1987A was the nearest detected SN of the modern era and is the best-studied event. Its progenitor star (Sk $-69°202$) in the LMC was a compact blue supergiant (B3 I; Gilmozzi et al. 1987; Sonneborn et al. 1987) inferred to have a mass close to $20\,\mathrm{M_\odot}$ (see Arnett et al. 1989 for a review). The size of the progenitor ($\lesssim 100\,\mathrm{R_\odot}$) was significantly smaller than those of average red supergiants (500–$1000\,\mathrm{R_\odot}$), and accounts for the slowly rising light curve. Pastorello et al. (2012) suggest that all known SN 1987A-like SNe are consistent with explosions of blue supergiant progenitors with radii between 35 and $90\,\mathrm{R_\odot}$ and masses at explosion of $\sim 20\,\mathrm{M_\odot}$, which would be higher, on average, than those identified for SN IIP progenitors (Smartt et al. 2009b).

For assumed values of the magnification, SN Refsdal had a high luminosity in comparison to well-studied low-redshift SN 1987A-like SNe (Pastorello et al. 2005; Kleiser et al. 2011; Taddia et al. 2012; Pastorello et al. 2012). We find that the $V - R$ color of SN Refsdal is similar to those of low-redshift SN 1987A-like SNe, but that it has a comparatively blue $B - V$ color, especially near maximum light. Scaling from a model of SN 1987A and using the fact that SN 1987A-like SNe exhibit a relatively small range of rise times, we estimate an ejecta mass of $20 \pm 5\,\mathrm{M_\odot}$ for the explosion.

We note that circumstellar interaction can range in intensity from very weak to very strong depending on the distribution, mass, and composition of any material surrounding the star. In the case of PTF 11iqb, for example, the CSM was overtaken early by the expanding ejecta and early narrow lines disappeared (Smith et al. 2015). Despite the lack of narrow lines near maximum light in spectra of PTF 11iqb, the CSM likely caused the SN to have a bluer color and higher luminosity.

Indeed, SN 1987A is surrounded by a ring thought to have been ejected approximately 10^4 yr before the explosion (Meaburn et al. 1995; Crotts & Heathcote 2000). Smith et al. (2014) have found that the light curves and spectra of the Type IIn SN 2009ip and SN 2010mc could be explained by the faint SN 1987A-like explosions of blue supergiant progenitors into dense CSM. It is possible that a small or even modest amount of circumstellar interaction could contribute to the color and luminosity of SN Refsdal that we observe.

Ongoing late-time *HST* imaging of the four images of SN Refsdal (PI P. Kelly; GO-14199) will continue to improve our understanding of the SN. As predicted (Kelly et al. 2015b; Oguri 2015; Sharon & Johnson 2015; Diego et al. 2015; Jauzac et al. 2015; Treu et al. 2015a; Grillo et al. 2015; Kawamata et al. 2015), SN Refsdal has reappeared in a different image of its spiral host galaxy (Kelly et al. 2015a). While other faded SNe depart forever, we will have a second opportunity to study SN Refsdal and to learn about its early evolution.
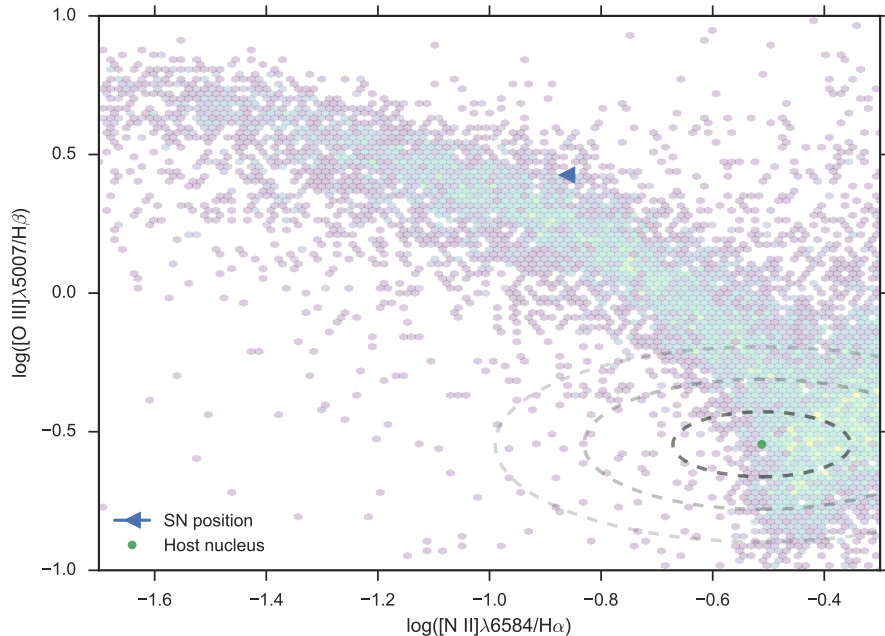
Figure 15. BPT diagram (Baldwin et al. 1981) for the emission lines measured from two host-galaxy extractions. The green dot shows the ratios for the host nuclear region, where the ellipses correspond to 1σ, 2σ, and 3σ confidence contours. The blue triangle marks the ratios of emission lines originating from near the SN position, where only an upper limit for [N II] flux could be estimated. This turns into an upper limit on the $\log(\text{[N II]}/\text{H}\alpha)$ ratio. Underplotted is the same ratio for all the $z \leq 0.1$ objects in the SDSS DR12 (Thomas et al. 2013).

REFERENCES

Akaike, H. 1974, IEEE T. Automat. Contr., 19, 716
Anderson, J. P., Covarrubias, R. A., James, P. A., Hamuy, M., & Habergham, S. M. 2010, MNRAS, 407, 2660
Applegate, D. E., von der Linden, A., Kelly, P. L., et al. 2014, MNRAS, 439, 48
Arnett, W. D. 1979, ApJ, 230, L37
Arnett, W. D., Bahcall, J. N., Kirshner, R. P., & Woosley, S. E. 1989, ARA&A, 27, 629
Baldwin, J. A., Phillips, M. M., & Terlevich, R. 1981, PASP, 93, 5
Barbon, R., Ciatti, F., & Rosino, L. 1979, A&A, 72, 287
Blinnikov, S., Lundqvist, P., Bartunov, O., Nomoto, K., & Iwamoto, K. 2000, ApJ, 532, 1132
Brammer, G. B., van Dokkum, P. G., Franx, M., et al. 2012a, ApJS, 200, 13
Brammer, G. B., Sánchez-Janssen, R., Labbé, I., et al. 2012b, ApJ, 758, L17
Chugai, N. N. 2001, MNRAS, 326, 1448
Cooper, M. C., Newman, J. A., Davis, M., Finkbeiner, D. P., & Gerke, B. F. 2012, spec2d: DEEP2 DEIMOS Spectral Pipeline, Astrophysics Source Code Library, ascl:1203.003
Crotts, A. P. S., & Heathcote, S. R. 2000, ApJ, 528, 426
Diego, J. M., Broadhurst, T., Chen, C., et al. 2015, ArXiv e-prints, arXiv:1504.05953
Doggett, J. B., & Branch, D. 1985, AJ, 90, 2303
Domínguez, A., Siana, B., Henry, A. L., et al. 2013, ApJ, 763, 145
Ebeling, H., Edge, A. C., & Henry, J. P. 2001, ApJ, 553, 668
Faber, S. M., Phillips, A. C., Kibrick, R. I., et al. 2003, in Society of Photo-Optical Instrumentation Engineers (SPIE) Conference Series, Vol. 4841, Instrument Design and Performance for Optical/Infrared Ground-based Telescopes, ed. M. Iye & A. F. M. Moorwood, 1657

Filippenko, A. V. 1982, PASP, 94, 715

—. 1997, ARA&A, 35, 309

Freudling, W., Romaniello, M., Bramich, D. M., et al. 2013, A&A, 559, A96

Gilmozzi, R., Cassatella, A., Clavel, J., et al. 1987, Nature, 328, 318

Gonzaga, S. e. 2012, The DrizzlePac Handbook

Grillo, C., Karman, W., Suyu, S. H., et al. 2015, ArXiv e-prints, arXiv:1511.04093

Hamuy, M., & Suntzeff, N. B. 1990, AJ, 99, 1146

Hamuy, M., Suntzeff, N. B., Heathcote, S. R., et al. 1994, PASP, 106, 566

Howell, D. A., Sullivan, M., Perrett, K., et al. 2005, ApJ, 634, 1190

Jauzac, M., Richard, J., Limousin, M., et al. 2015, ArXiv e-prints, arXiv:1509.08914

Karman, W., Grillo, C., Balestra, I., et al. 2016, A&A, 585, A27

Kass, R. E., & Raftery, A. E. 1995, J. Amer. Amer. Stat. Assn., 90, 773

Kawamata, R., Oguri, M., Ishigaki, M., Shimasaku, K., & Ouchi, M. 2015, ArXiv e-prints, arXiv:1510.06400

Kelly, P. L., & Kirshner, R. P. 2012, ApJ, 759, 107

Kelly, P. L., Kirshner, R. P., & Pahre, M. 2008, ApJ, 687, 1201

Kelly, P. L., von der Linden, A., Applegate, D. E., et al. 2014, MNRAS, 439, 28

Kelly, P. L., Rodney, S. A., Treu, T., et al. 2015a, ArXiv e-prints, arXiv:1512.04654

—. 2015b, Science, 347, 1123

Kiewe, M., Gal-Yam, A., Arcavi, I., et al. 2012, ApJ, 744, 10

Kleiser, I. K. W., Poznanski, D., Kasen, D., et al. 2011, MNRAS, 415, 372

Larkin, J., Barczys, M., Krabbe, A., et al. 2006, in Society of Photo-Optical Instrumentation Engineers (SPIE) Conference Series, Vol. 6269, 1

McLean, I. S., Steidel, C. C., Epps, H., et al. 2010, in Society of Photo-Optical Instrumentation Engineers (SPIE) Conference Series, Vol. 7735, 1

McLean, I. S., Steidel, C. C., Epps, H. W., et al. 2012, in Society of Photo-Optical Instrumentation Engineers (SPIE) Conference Series, Vol. 8446, 0

Meaburn, J., Bryce, M., & Holloway, A. J. 1995, A&A, 299, L1

Modigliani, A., Goldoni, P., Royer, F., et al. 2010, in Society of Photo-Optical Instrumentation Engineers (SPIE) Conference Series, Vol. 7737, 28

Momcheva, I. G., Brammer, G. B., van Dokkum, P. G., et al. 2015, ArXiv e-prints, arXiv:1510.02106

Mukherjee, S., Feigelson, E. D., Jogesh Babu, G., et al. 1998, ApJ, 508, 314

Newman, J. A., Cooper, M. C., Davis, M., et al. 2013, ApJS, 208, 5

Oguri, M. 2015, MNRAS, 449, L86

Pagel, B. E. J., Edmunds, M. G., Blackwell, D. E., Chun, M. S., & Smith, G. 1979, MNRAS, 189, 95

Pastorello, A., Baron, E., Branch, D., et al. 2005, MNRAS, 360, 950

Pastorello, A., Pumo, M. L., Navasardyan, H., et al. 2012, A&A, 537, A141

Pettini, M., & Pagel, B. E. J. 2004, MNRAS, 348, L59

Phillips, M. M., Hamuy, M., Heathcote, S. R., Suntzeff, N. B., & Kirhakos, S. 1990, AJ, 99, 1133

Phillips, M. M., Heathcote, S. R., Hamuy, M., & Navarrete, M. 1988, AJ, 95, 1087

Reddy, N. A., Kriek, M., Shapley, A. E., et al. 2015, ApJ, 806, 259

Refsdal, S. 1964, MNRAS, 128, 307

Rodney, S. A., Strolger, L.-G., Kelly, P. L., et al. 2015, ArXiv e-prints, arXiv:1512.05734

Schlafly, E. F., & Finkbeiner, D. P. 2011, ApJ, 737, 103

Schmidt, K. B., Treu, T., Brammer, G. B., et al. 2014, ApJ, 782, L36

Sharon, K., & Johnson, T. L. 2015, ApJ, 800, L26

Silverman, J. M., Foley, R. J., Filippenko, A. V., et al. 2012, MNRAS, 425, 1789

Smartt, S. J., Eldridge, J. J., Crockett, R. M., & Maund, J. R. 2009a, MNRAS, 395, 1409

—. 2009b, MNRAS, 395, 1409

Smith, G. P., Ebeling, H., Limousin, M., et al. 2009, ApJ, 707, L163

Smith, N., Chornock, R., Silverman, J. M., Filippenko, A. V., & Foley, R. J. 2010, ApJ, 709, 856

Smith, N., Mauerhan, J. C., & Prieto, J. L. 2014, MNRAS, 438, 1191

Smith, N., Mauerhan, J. C., Cenko, S. B., et al. 2015, MNRAS, 449, 1876

Sonneborn, G., Altner, B., & Kirshner, R. P. 1987, ApJ, 323, L35

Staveley-Smith, L., Kim, S., Calabretta, M. R., Haynes, R. F., & Kesteven, M. J. 2003, MNRAS, 339, 87

Sugiura, N. 1978, Commun. Stat. A-Theor., 13

Taddia, F., Stritzinger, M. D., Sollerman, J., et al. 2012, A&A, 537, A140

Taddia, F., Sollerman, J., Razza, A., et al. 2013, A&A, 558, A143

Thomas, D., Steele, O., Maraston, C., et al. 2013, MNRAS, 431, 1383

Tonry, J., & Davis, M. 1979, AJ, 84, 1511

Treu, T., & Ellis, R. S. 2015, ConPh, 56, 17

Treu, T., Brammer, G., Diego, J. M., et al. 2015a, ArXiv e-prints, arXiv:1510.05750

Treu, T., Schmidt, K. B., Brammer, G. B., et al. 2015b, ApJ, 812, 114

Vernet, J., Kerber, F., Mainieri, V., et al. 2010, Highlights of Astronomy, 15, 535

Vernet, J., Dekker, H., D'Odorico, S., et al. 2011, A&A, 536, A105

von der Linden, A., Allen, M. T., Applegate, D. E., et al. 2014, MNRAS, 439, 2

Welty, D. E., Xue, R., & Wong, T. 2012, ApJ, 745, 173

Yaron, O., & Gal-Yam, A. 2012, PASP, 124, 668

Yuan, T., Kobayashi, C., & Kewley, L. J. 2015, ApJ, 804, L14

Yuan, T.-T., Kewley, L. J., Swinbank, A. M., Richard, J., & Livermore, R. C. 2011, ApJ, 732, L14

Zitrin, A., & Broadhurst, T. 2009, ApJ, 703, L132

APPENDIX

METHODS

(1) Phases of the MOSFIRE, WFC3, and X-shooter Spectra Relative to Time of Maximum Light

The mean phase relative to maximum light (in the SN rest frame) of the Keck-I MOSFIRE data is -62 ± 8 d, of the *HST* WFC3 G141 grism spectra is -47 ± 8 d, and of the VLT X-shooter spectra is $+16 \pm 8$ d. At maximum light, $F160W \approx 24.45$ mag AB for image S2.

(2) HST WFC3-IR G141 Grism Data

(a) Processing

We processed the WFC3/IR FLT images obtained from the *HST* archive using the software pipeline developed for the 3D-HST project[23] (Brammer et al. 2012a). This pipeline employs the `DrizzlePac` package (Gonzaga 2012)[24] to

---

[23] https://github.com/gbrammer/threedhst

[24] http://adsabs.harvard.edu/abs/201two-dimensionalrzp.book.....G

align the WFC3 images, and a custom software package to extract and model the grism spectra (Brammer et al. 2012b; Momcheva et al. 2015)[25][26].

(b) Modeling Contaminant Spectroscopic Traces

In a grism spectral element, light passes first through a prism and then a diffraction grating. The light from all objects in the field is dispersed in a common direction, making efficient spectroscopy of a large number of objects possible. The Einstein cross, however, presents a challenge for grism spectroscopy, because the SN images are embedded in light from both the spiral host galaxy and the early-type galaxy lens. In Figure 16, we show a coaddition of all $F125W$ and $F160W$ direct exposures of the SN images S1–S4, adjacent sources, and the dimensions of the first-order and second-order grism traces. The traces of nearby, bright cluster members create additional strong contamination, and a nearby bright star with $r = 15.1$ mag AB produces strong diffraction spikes.

The roll angle of the spacecraft determines the dispersion axis of the WFC3 G141 grism. Acquiring spectra at more than one roll angle makes possible a more robust extraction, because the trace at each roll angle is contaminated by different sources. To identify the two combinations of roll angles and SN images that would yield the least contamination, we simulated the expected grism spectra at all roll angles available at the time of the observation, and predicted that image S2 observed at angles 111° and 119° would be least contaminated.

Even after configuring the observations to obtain the cleanest possible SN spectra, light from other sources accounts for 85–90% of the light along the traces of image S2 of SN Refsdal. To recover the SN spectrum, we constructed and subtracted models of overlapping traces. We used the wide-band $F125W - F160W$ color and the $F160W$ flux to model the continuum of the spiral host galaxy, the $z = 0.54$ elliptical cluster-member lens, and the two adjacent red-sequence cluster members. We used the $F160W$ flux to model the Hα and [O III] narrow-line emission from the $z = 1.49$ spiral host galaxy. Figure 17 shows the two-dimensional models for the contaminating sources. Finally, we subtracted the residual background measured within a parallel adjacent aperture. Figure 18 shows the successive removal of the modeled sources and the parallel background measurement for the grism spectrum taken in the 111° telescope orientation. In Figure 2, we plot the extracted spectra of image S2 in orients 111° and 119°, and, for comparison, that of SN 1987A at the same epoch.

(c) Rejecting Outlying Flux Measurements

We compute a smoothed spectrum at the wavelength of each measurement with a weight proportional to a Gaussian density with $\sigma = 3000\,\mathrm{km\,s^{-1}}$ in the rest frame and inversely proportional to the square of the uncertainty of the flux measurement (Tonry & Davis 1979). The narrow lines have already been removed during an earlier processing step.

(d) Comparison Between Direct Imaging Magnitudes and Grism Spectra

Given the fact that the SN flux was only a small fraction of the contaminating flux along the trace, a useful consistency check is to assess how well synthetic magnitudes calculated from the grism SN spectrum agree with direct photometry of the SN. We compute synthetic AB magnitudes using the $F125W$ and $F160W$ filter functions, and calculate a synthetic $F125W - F160W$ color.

The grism spectra were taken from December 23, 2014 through January 5, 2015, but all of the 202.9 s post-imaging exposures were taken with the $F160W$ wide-band filter from 23–28 December, while all post-imaging exposures from 30 December 2014 through 4 January 2015 was taken with the $F125W$ wide-band filter. To estimate the average color of SN Refsdal during the period of grism observations, we have coadded post-imaging exposures acquired on December 28–31, 2014, when coverage spans approximately the same epochs. These dates bracket the midpoint of the grism observations on December 29, 2014.

We measure direct magnitudes of $F125W = 25.01 \pm 0.05$ mag AB and $F160W = 25.06 \pm 0.05$ mag, or a color of $F125W - F160W = -0.05 \pm 0.07$ mag AB. Then we calculate a synthetic color of $F125W - F160W = 0.14$ mag AB.

(3) VLT X-shooter Spectroscopy

The VLT data were reduced using the ESO/X-shooter pipeline v2.5.2 (Modigliani et al. 2010), where the Reflex interface (Freudling et al. 2013) is used to manage the pipeline. The two-dimensional spectra have been rectified on a grid with $0.2\,\text{\AA}\,\mathrm{pix}^{-1}$ in the ultraviolet blue (UVB) and VIS and $0.6\,\text{\AA}\,\mathrm{pix}^{-1}$ in the NIR arm, slightly oversampling the spectra given the nominal X-shooter resolving power. The spectra are flux calibrated using an observation of a spectrophotometric standard (Vernet et al. 2010; Hamuy et al. 1994) from which we measure a response function.

The cluster field in which data were taken contains light from the $z = 1.49$ spiral host galaxy and cluster galaxies in the off-region locations observed during the nodding sequence. The continua of these sources are relatively featureless near the Hα emission from the SN, so we do not expect subtraction of the emission from these contaminants to affect the VLT SN spectrum. While there is no evidence of subtraction of significant narrow-line nebular emission for OB1 and OB2, line emission in the "off region" used for OB3 contains strong emission, and we do not use the spectra acquired during this OB when estimating emission-line strengths. A reduction in stare mode has also been carried out, where the sky is estimated using a sigma-clipped mean in the regions free of host-galaxy light. The noise images for both reduction modes are constructed directly from the data at each wavelength bin where the standard deviation is calculated in the regions excluding the host.

---

[25] http://adsabs.harvard.edu/abs/2012ApJ...758L..17B

[26] http://adsabs.harvard.edu/abs/2015arXiv151002106M

The positions of the SN images on the slit were determined by measuring the distance from the host nucleus in the *HST* image. Hα emission from the host nucleus is clearly visible in the two-dimensional spectrum.

(a) Extraction and Combination

We have extracted two separate sets of spectra to study the SN and to examine the strong nebular emission. To study the SN light, we use a 6 pixel (1$''$08) wide aperture centered at the positions of the SN. We use a model of sky lines from ESO[27] to construct a mask of strong night-sky emission. In addition to line emission, the sky also produces continuum emission, and we model and subtract the continuum emission by computing the median value in bins of 200 Å in wavelength, after removing pixel elements with radiance $> 20{,}000$ photons s^{-1} m^{-2} μm^{-1} arcsec^{-2}. After subtracting the continuum emission from the sky, we interpolate the background-subtracted sky spectrum to the X-shooter wavelength grid and mask pixels with sky values greater than 10,000 photons s^{-1} m^{-2} μm^{-1} arcsec^{-2} when binning. We also mask any pixels within 6.4 Å (5σ) of a strong nebular emission line, including Hα and [N II]. To study the host-galaxy narrow-line emission, we instead extract using an aperture with a width that is 250% of the average FWHM seeing listed in Table 3.

For both sets of extractions, the flux in each aperture is summed, and the noise spectrum within the same aperture is added in quadrature. We next apply aperture corrections appropriate for the SN point source. To estimate the expected slit loss for the SN and contamination from the early-type lens and host galaxy, we convolve a pre-explosion *HST* WFC3 *F*160*W* image with a Gaussian kernel to produce an image having the average FWHM expected during each X-shooter observation (see Table 3). From the position angle and target positions, we next create pixel masks of the slit apertures. We use these masks and the convolved images to calculate the average expected SN and galaxy light admitted through the slit. We correct each spectrum for the slit losses appropriate for the SN point source.

We smooth each of the OBs separately and remove 5σ outliers. The spectra are finally combined using a weighted average, and we propagate uncertainties.

(4) Estimating the Luminosity of the SN Hα Emission

We measure the Hα strength by fitting a Gaussian to the emission after subtracting a continuum level. We estimate a median flux in the wavelength range 14,500–15,500 Å for the grism spectrum. In the case of the X-shooter data, the continuum estimate is the median of the flux in the range 15,300–15,600 Å and 16,500–17,000 Å. The uncertainty is computed by repeating this procedure to the bootstrap-resampled spectra.

To assemble the comparison plot in Figure 11, we renormalize the SN 1987A-like SNe and SN 2005cp comparison spectra to match published total magnitudes in the papers listed in Table 6. We next correct the spectra to remove Milky Way and host-galaxy reddening according to the values in Table 6 and shift the comparison spectra to the rest frame. The spectra of the low-redshift comparison SNe have high S/N, and we estimate the continuum visually from the region adjacent to their P-Cygni Hα profiles while avoiding the Ba II λ6142 feature.

(a) Nebular Emission from Near the SN Position and Host Nuclear Region

We identify the host-galaxy emission lines [O II] λ3727, Hγ, Hβ, [O III] λ4959, [O III] λ5007, Hα, [N II] λ6584, [S II] λ6716, and [S II] λ6731 with varying statistical significance. Narrow lines are detected across much of the spatial direction of the slit, which extends along both the host nucleus and position of SN images S1 and S2 for observations OB1 and OB2 and the position of SN images S2 and S3 for OB3. As an illustration, Figure 14 shows the detection of [O II] in OB2. The spatial dimension of the slit allows us to determine both the conditions local to the SN and within the nuclear region.

Parameters useful for the determination of the conditions of the emitting gas are the fluxes and widths of the strong nebular emission lines. Strong-line diagnostics using the measured line fluxes can then be used to infer the oxygen abundance of the emitting gas.

To estimate the uncertainty of the strong-line fluxes, we create bootstrapped spectra from the set of four separate spectra of images of the explosion site assembled from the OB1 and OB2 observations of SN images S1 and S2. Unlike the spectra taken during OB3, the spectra acquired in OB1 and OB2 show no evidence that emitting sources in the "off regions" were subtracted from the spectrum of the "on regions."

For each of the bootstrapped samples, the lines of [O II] λ3727, Hβ, [O III] λ4959, [O III] λ5007, Hα, and [N II] λ6584 are fit using weighted least-squares, where for the [O II] and [O III] doublets the widths are required to be the same, and the position and width of [N II] are determined from the fit to [O III] λ5007 which is not contaminated by night-sky emission. We use the inverse variance as the weight. To estimate the uncertainty of the individual fits, we fit the spectrum assembled from each bootstrap combination 100 times after resampling within the uncertainty. We use the mean and the standard deviation of the resulting distribution to estimate the value and uncertainty of the line flux.

We do not detect [N II] in the spectrum extracted at the SN position, so we instead report an upper limit. To determine the value of the upper limit, we add an artificial line of increasing strength with a width matching that of the well-detected [O III] λ5007 and repeat until we obtain a 3σ detection.

For the host-galaxy nuclear region, we only have two extractions from OB1 and OB2, so we find a weighted combination of the two independent extractions. Because the strength of [O III] λ5007 is weak at the position of the

---

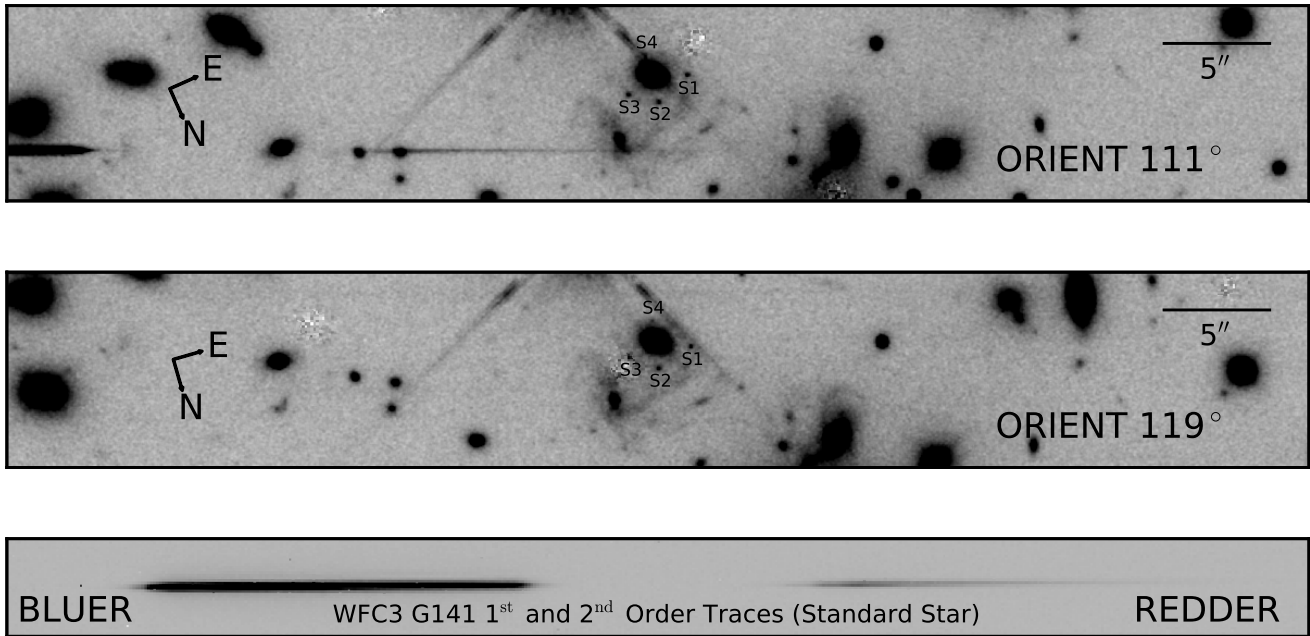[27] http://www.eso.org/observing/etc/skycalc/skycalc.htm

Figure 16. Coaddition of WFC3/IR $F125W$ and $F160W$ exposures taken before G141 grism integrations at the same orientation. The dispersion axis is horizontal. Unlike with a prism, blue light makes a smaller relative angle with the grism. The first-order trace spans 11,000–17,000 Å (~ 4400–6800 Å in the SN rest frame). Bottom panel shows the first- and second-order traces in an observation of the standard star GD-153 (GO-13092; PI J. Lee).

host-galaxy nucleus, we use the width of [O II] instead of [O III] as a model for [N II] and let it vary within 3σ of the best-fit values for [O II]. Using [O II] or [O III] to model the [N II] line profile has only a $\sim 5\%$ effect on measured emission-line ratios.
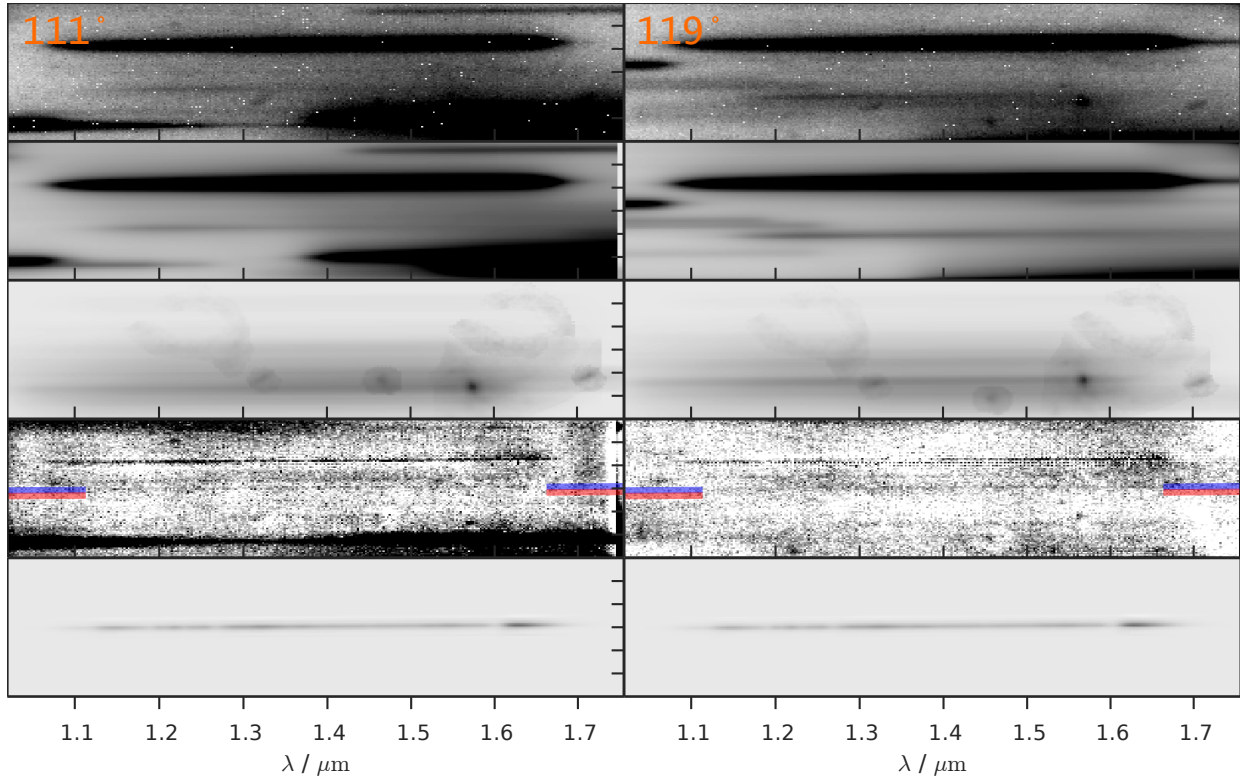
Figure 17. WFC3 G141 two-dimensional grism spectra taken of SN Refsdal in the 111° and 119° orientations. For each orientation (beginning from the top), the first panel shows the full observed spectrum, the second panel gives a model of nearby contaminants, the third panel provides the model of the Hα and [O III] emission lines, and the fourth panel is the cleaned residual spectrum, with the stretch now 10 times that of the preceding panels. The final panel is the model two-dimensional spectrum of the SN IIP template. Blue bands show the extraction region of the S2 trace itself (it continues across the whole spectrum but is only shown at the edges, so one can actually see the spectrum under it) and the red band is the adjacent aperture used for the local background. The tick marks on the ordinate axis are spaced by 1″
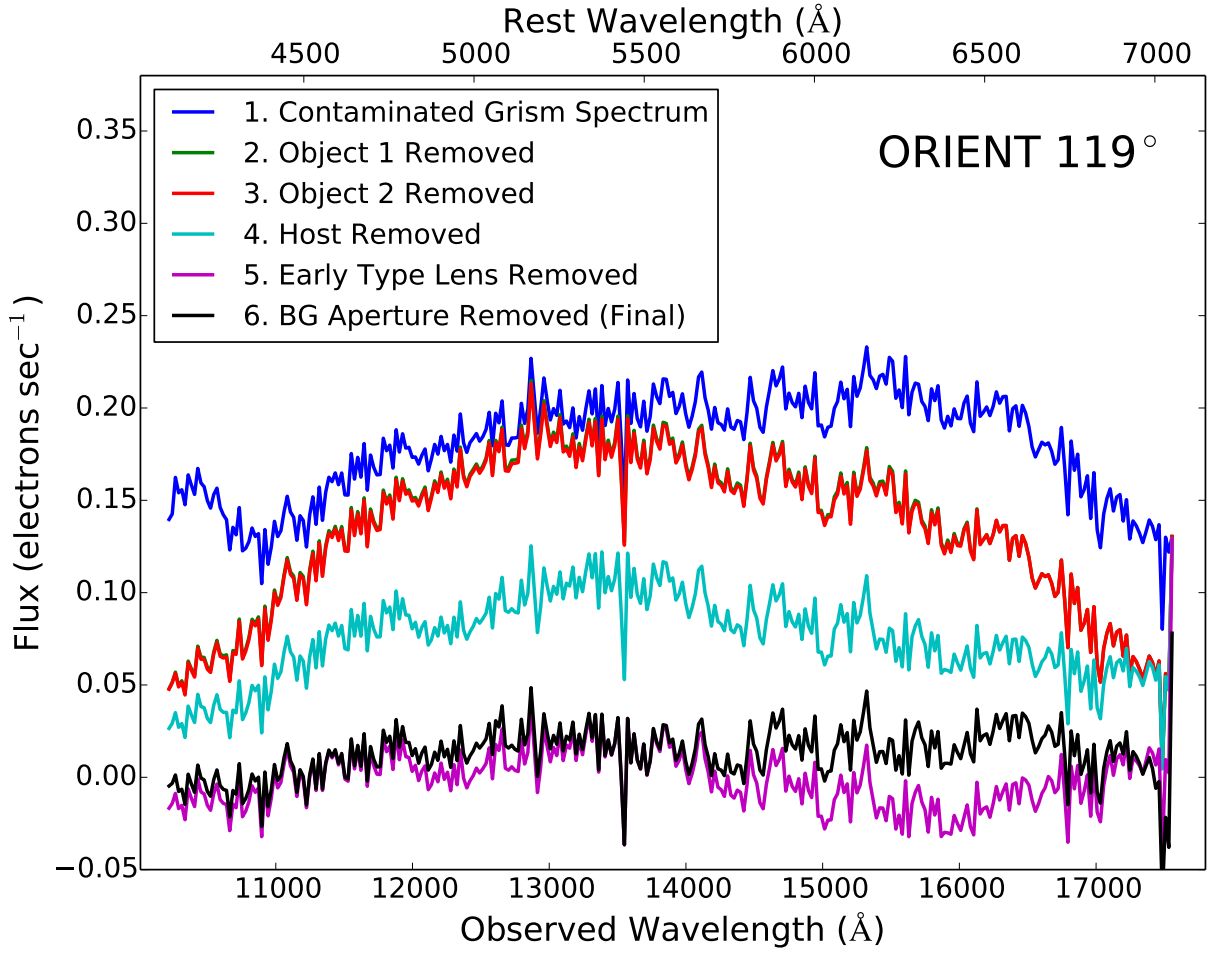
Figure 18. Successive subtraction of contamination along the WFC3 grism trace of SN Refsdal taken in the the 119° telescope orientation. The light from SN Refsdal constitutes only 10–15% of the light in the extraction aperture. The steps follow in parallel the order of panels from top to bottom in Fig. 17. The background subtraction ("BG Aperture") is the flux measured in an aperture running parallel to the extraction aperture. Background removal corrects a modest overcorrection for contamination at redder wavelengths. Despite extremely strong contamination, synthetic magnitudes of the subtracted spectrum yield a $F125W - F160W$ color that has reasonable agreement with magnitudes measured from direct imaging (see Section A.2.4). The level of contamination along of trace of image S2 in the grism spectrum acquired at 111° orient is comparable.
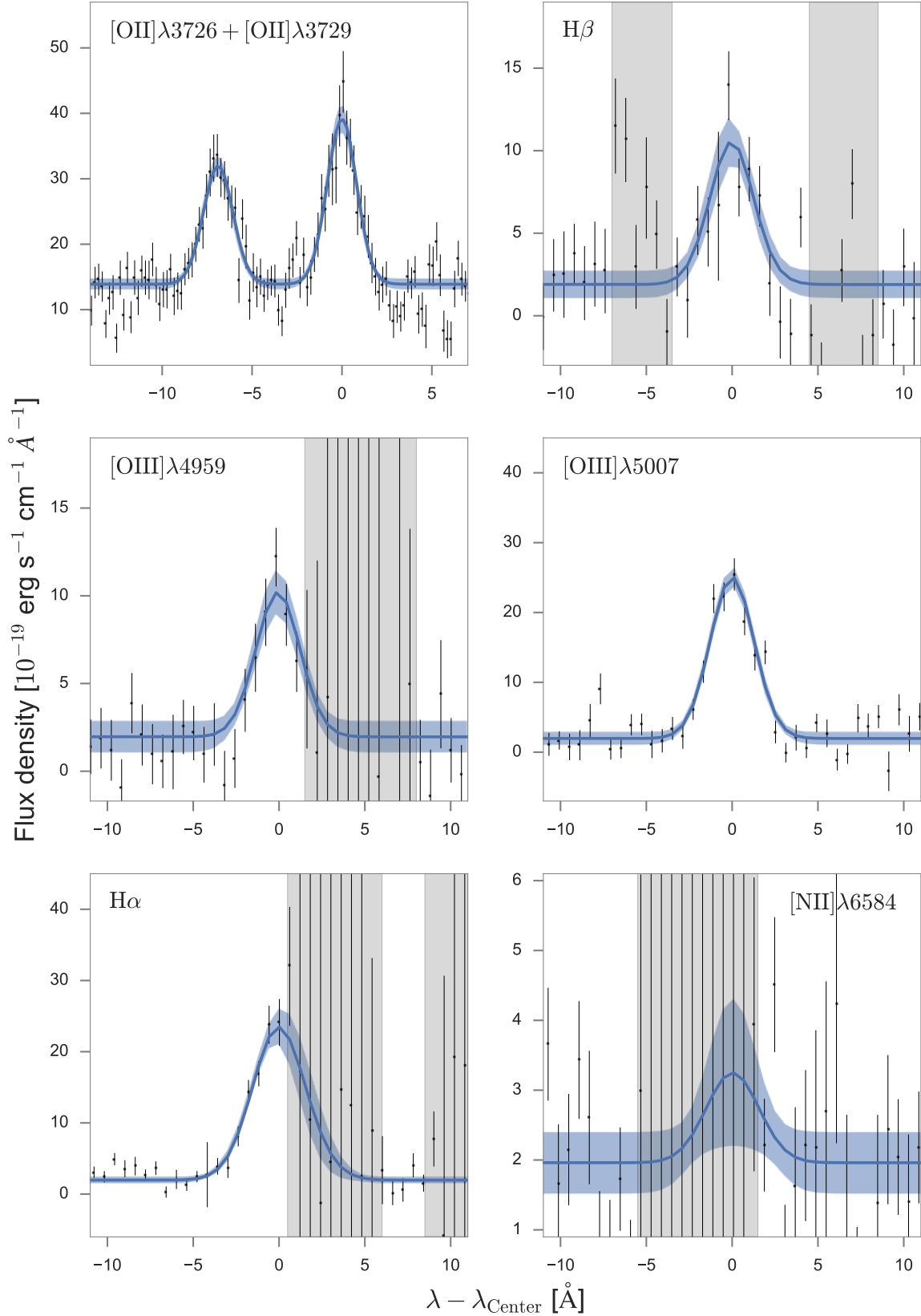
Figure 19. Profiles of narrow emission lines in X-shooter spectra at positions of SN images. Each fitted model (blue) consist of a Gaussian profile and a constant background. Regions having strong sky background from emission lines are shown by the gray background. Here we first find μ and σ that yield the best fit to the [O III] $\lambda5007$ emission line, and, during fits to other emission lines, we allow the line amplitude and local background to vary. The widths of the emission lines arising from forbidden transitions ([O III] $\lambda\lambda4959$, 5007) and permitted transitions (Hα and Hβ) are comparable, which suggests that the narrow-line emission arises from H II regions instead of from the SN.